

HAT Variability Survey in the High Stellar Density “Kepler Field” with Millimagnitude Image Subtraction Photometry.

J. D. Hartman, G. Bakos^{1,2}, K. Z. Stanek, R. W. Noyes

Harvard-Smithsonian Center for Astrophysics, 60 Garden St., Cambridge, MA 02138

jhartman, gbakos, kstanek, rnoyes@cfa.harvard.edu

ABSTRACT

The Hungarian-made Automated Telescope network (HATnet) is an ongoing project to detect transiting extra-solar planets using small aperture, robotic telescopes. In this paper we present the results from using image subtraction photometry to reduce a crowded stellar field (chosen to overlap with the planned *Kepler* mission). We obtained I-band light curves for 98,000 objects in a 67-square-degree field of view centered at $(\alpha, \delta) = (19^{\text{h}}44^{\text{m}}00^{\text{s}}.0, +37^{\circ}32'00''.0)$ (J2000.0), near the Galactic plane in the constellations Cygnus and Lyra. These observations include 788 5-minute exposures over 30 days. For the brightest stars ($I \sim 8.0$) we achieved a precision of 3.5 millimagnitudes, falling to 0.1 magnitudes at the faint end ($I \sim 14$). From these light curves we identify 1617 variable stars, of which 1489 are newly discovered. The fact that $> 90\%$ of the variables were previously undetected further demonstrates the vast number of variables yet to be discovered even among fairly bright stars in our Galaxy. We also discuss some of the most interesting cases. This includes: V1171 Cyg, a triple system with the inner two stars in a $P = 1.462$ day period eclipsing orbit and the outer star a $P = 4.86$ day Cepheid; HD227269, an eccentric eclipsing system with a $P = 4.86$ day period that also shows $P = 2.907$ day pulsations; WW Cyg, a well studied eclipsing binary; V482 Cyg, an RCB star; and V546 Cyg, a PV Tel variable. We also detect a number of small amplitude variables, in some cases with full amplitude as low as 10 mmag.

Subject headings: techniques: photometric — catalogs — binaries: eclipsing – Cepheids — delta Scuti — stars: variables: other

1. Introduction

The Hungarian-made Automated Telescope network (HATnet) is an ongoing project to detect transiting extra-solar planets using small aperture, robotic telescopes (Bakos et al. 2004, hereafter

¹Predoctoral Fellow, Smithsonian Astrophysical Observatory

²Also at Konkoly Observatory, Budapest, H-1525, P.O. Box 67

B04). The HATnet telescopes make use of a fast focal ratio ($f/1.8$) to efficiently monitor a large number of fairly bright stars ($I < 14.5$) over a wide field-of-view (FOV). A number of other groups have also taken this small-telescope approach toward finding transits (see Horne 2003 for a comprehensive list). In contrast, there are several groups that employ a “narrow, but deep” method. This includes the transit search by the Optical Gravitational Lensing Experiment (OGLE) project, which to date has discovered three confirmed “very hot Jupiters” (Udalski et al. 2002, 2003; Konacki et al. 2003; Torres et al. 2004; Bouchy et al. 2004; Konacki et al. 2004), the only planets detected so far by transit searches.

Besides the size of the telescopes and FOV, another difference between the approaches is the method used to obtain photometry for the monitored stars. For several years many of the “narrow and deep” searches have made use of the image subtraction techniques due to Alard & Lupton (1998; also Alard 2000). This includes OGLE which uses Difference Image Analysis (DIA, Wozniak 2000), and PISCES (Mochejska et al. 2002, 2004) which uses a different implementation of image subtraction in monitoring the open clusters NGC 2158 & NGC 6791.

Image subtraction is the current state of the art for massive time-series photometry. It has been shown that in narrow, dense fields, it can produce light curves with precision down to the photon limit (e.g. see Mochejska et al. 2002). However, to date there exists no published results that use image subtraction in a wide-field setting. This has limited these searches to observing only relatively isolated stars in regions where point spread function (PSF) fitting and aperture photometry yield high precision.

In this paper we report our use of image subtraction to obtain light curves for 98,000 objects in a single field, near the galactic plane. This field was chosen in particular because of its overlap with NASA’s *Kepler* mission to observe transiting planets from space (Borucki et al. 2003). Over 9,000 of the brightest light curves have a root-mean-square (RMS) of less than 1% (i.e. better than 10 millimagnitude precision) at 5-min sampling. In the following section we describe our observations, and in §3 we discuss our image subtraction based data reduction to obtain the light curves.

While the main purpose of HATnet remains the discovery of transiting extra-solar planets, it is also useful for discovering and characterizing variable stars in the Galaxy. To this end we have analyzed these light curves to select a list of 1617 variable stars, of which 1489 are newly discovered. We describe our selection criteria in §4 and present our catalog, including a discussion of many interesting cases, in §5. We finish with a brief summary of our results in §6.

2. Observations

The data were obtained in June and July, 2003 using the HAT-5 telescope located at the Fred Lawrence Whipple Observatory (FLWO). The telescope uses a Canon 200 mm $f/1.8L$ lens and a Cousins I-band filter to image onto an Apogee AP10 front-illuminated, $2K \times 2K$ CCD. The result is an $8.3^\circ \times 8.3^\circ$ FOV image with a pixel scale of $14''$. For details on the design and performance of

the instrument see B04. The pointing was stepped in a prescribed pattern of sub-pixel increments during each exposure to broaden the full width at half maximum (FWHM) of the stellar profiles from ~ 1.5 pix to ~ 2.5 pix.

The field we observed (HAT-199) is centered at $(\alpha, \delta) = (19^{\text{h}}44^{\text{m}}00^{\text{s}}.0, +37^{\circ}32'00''.0)$ (J2000.0) and lies at the western boundary of the constellation Cygnus (Fig. 1). The south-eastern (lower left) corner of the field is within 2° of the Galactic plane. As mentioned above, this field was chosen to overlap with the proposed center for NASA’s *Kepler* Mission (D. Latham, private communication). Thus these observations may be useful as a means of identifying interesting objects (including stars bearing transiting planets) to be investigated at higher precision with *Kepler*.

This field contains hundreds of thousands of relatively bright sources, from which we select 98,000 with $I < 14.8$. Just from the sources we select the density is 0.4 objects per square-arcmin. At our pixel scale this corresponds to one object per 42 pixels, or a typical separation of 6-7 pixels between the objects. At this density the stellar profiles are highly blended, particularly toward the galactic plane (Fig. 2). Because of this severe blending, without image subtraction large portions of this field would not be useful for transit searches or precision photometry in general.

3. Data Reduction

3.1. Image Subtraction

The preliminary CCD reductions including dark current subtraction, flat-fielding, etc. were discussed in B04.

To obtain photometry we used the image subtraction methods due to Alard & Lupton (1998, also Alard 2000). We describe the procedure here, referring the reader interested in the theoretical basis of the method to the original papers.

The simplest method to measure the apparent magnitude of a star is to measure the total signal within a fixed aperture centered on the star. However, when one is working on a crowded stellar field this method breaks down since more than one source will contribute light to the aperture. The typical procedure in this case is to determine a PSF for the frame using bright/isolated stars, and then fit that PSF to all the stars on the frame.

When obtaining light curves for the stars in a dense field, it is possible to obtain even higher precision by noting that for the majority of stars the intrinsic magnitude will vary only slightly, if at all, from image to image. Instead of performing PSF fitting separately on every image, one can obtain higher precision by performing weighted aperture photometry on the sparsely populated difference image formed by subtracting the image from a reference image. To do this one needs a method for matching two images with different PSFs before subtracting so that the subtracted image is not dominated by residuals from the different PSFs. Alard & Lupton (1998) solved this

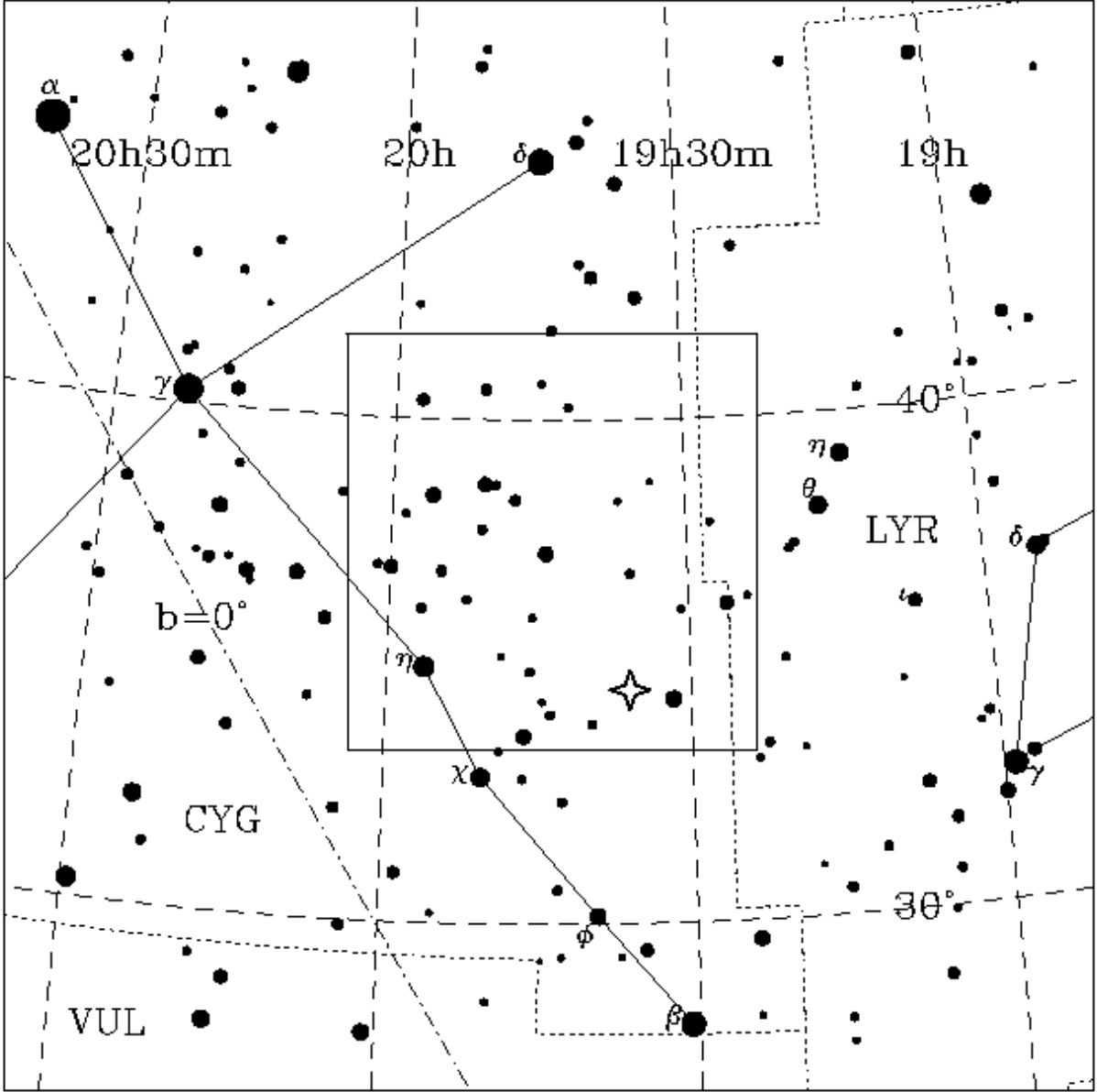


Fig. 1.— The observed $8.3^\circ \times 8.3^\circ$ field of view, lying at the western boundary of Cygnus. The proposed center of the *Kepler* Mission is marked with a star. The plane of the Galactic disk is shown with the dot-dashed line.

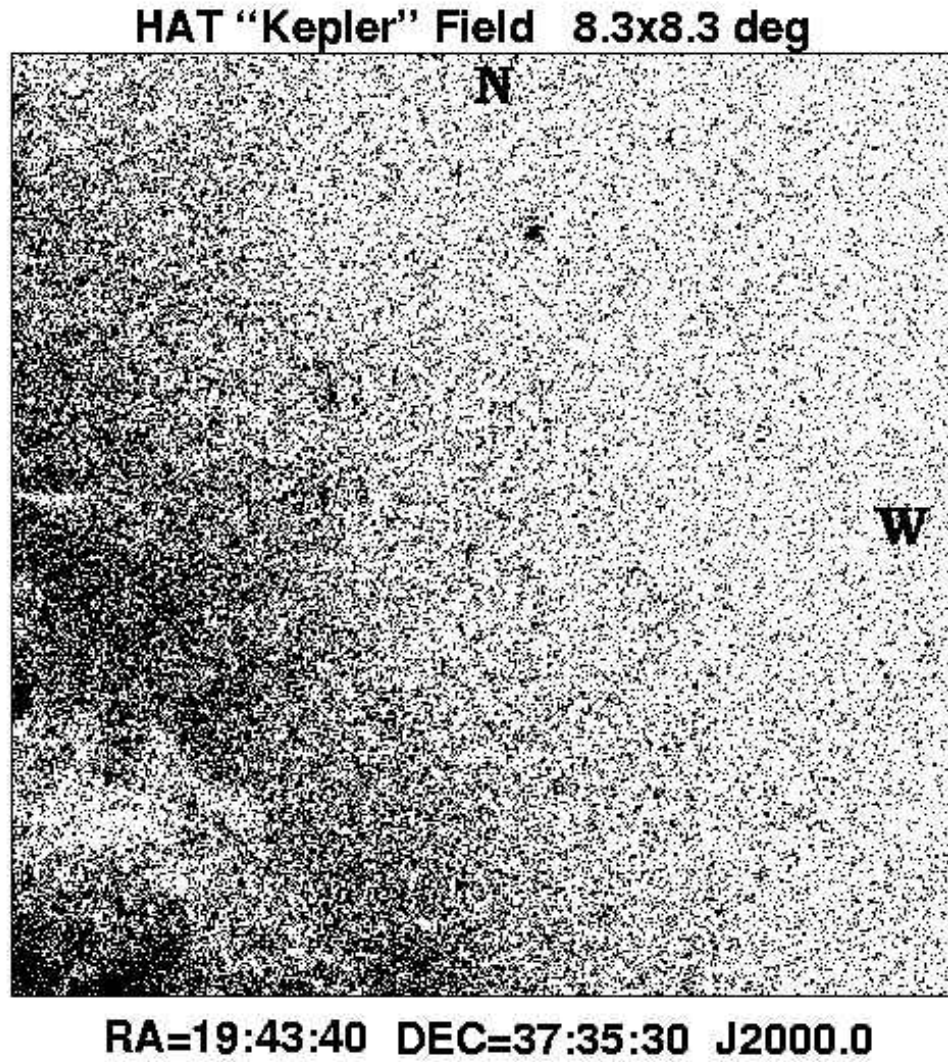


Fig. 2.— Image of the HAT “Kepler” field (HAT-199). Note the very high stellar density, and variable extinction, particularly toward the Galactic disk in the lower left corner.

problem by proposing an efficient method for finding a function that transforms the PSF of the reference image into the PSF of the image to be subtracted (the kernel). Their scheme does not assume anything about the shape of the PSF, only that the kernel, which relates the PSFs on different images, can be written in terms of a product of gaussians and polynomials (of arbitrary order). Alard (2000) modified the procedure to allow for spatial variations in the kernel which can be fit with a polynomial. When fitting the kernel it is not necessary to use only bright/isolated stars, instead even stars in the highest density regions contribute to the fit. This is one reason why the kernel can be obtained with better accuracy than an independent determination of the PSF. Another reason why the kernel can be determined with better accuracy than the PSF is that while the PSF can have an arbitrary shape that may not be well-fit by any model function, empirically the kernel relating two PSFs from the same instrument appears to be well-fit by Alard & Lupton’s model, regardless of the shape of the PSF. Moreover, because the kernel fitting procedure assumes that the majority of stars are not varying in intrinsic magnitude from image to image, any correlated variations such as the change in magnitude due to different atmospheric extinction are automatically removed.

Once the kernel is obtained and the images have been subtracted, it is a simple step to obtain the relative change in magnitude between the subtracted image and the reference image. This is done by determining a PSF for the reference image, convolving it with the kernel, and then performing weighted aperture photometry on the subtracted image.

All of the above procedures are included in the ISIS 2.1 package³. There are several references on how to run ISIS, the procedure we follow is similar to that used by Mochejska et al. (2002). We highlight here the steps that are unique to our survey.

To select a reference for alignment we measured the full-width at half-maximum (FWHM) values of all the images and then chose an image which had one of the smallest FWHMs, circular profiles, and had good spatial overlap with the remaining images. At this point we also examined images with extreme values for FWHM (typically frames for which the program failed). Many of these turned out to be partially obscured by clouds, or have irregular background patterns (due to zodiacal light, proximity to the moon, etc.). These images were removed before proceeding with registration/subtraction.

Before proceeding with subtraction we had to establish a set of subtraction parameters. These parameters include the number of independent regions in which to divide the images (`sub_x` and `sub_y`), the form of the kernel to use (including the number of gaussians, the “width” of the gaussians, the orders of the polynomials associated with each Gaussian, the order of the polynomial used to fit spatial variations in the kernel, and the order of the polynomial used to fit spatial variations in the background), and the sizes (in pixels) of the regions used for fitting the kernel (`half_stamp_size`) as well as for performing the PSF transformation with the kernel

³ISIS package is available from C. Alard’s website at <http://www2.iap.fr/users/alard/package.html>

(`half_mesh_size`). We first created a preliminary reference image from 30 of the lowest FWHM images, using a trial guess for the parameters. We then ran the ISIS routine “subtract.csh” using several permutations of the parameters (we varied the number of subregions, and the degree of background and spatial variations). For each permutation we calculated the standard deviation and mean of the subtracted images. We then chose the set of parameters which produced the lowest average standard deviation and mean. These include internally dividing each frame into 25 independent sub-frames (`sub_x = sub_y = 5`), using a first order polynomial to fit the background variations and first order polynomial to fit the spatial variations in the kernel, fitting with 3 gaussians, that had “widths” of 0.7, 2.0 and 4.0 respectively, and associated polynomials of order 6, 4 and 3 respectively, and choosing a `half_mesh_size` of 11 pixels and a `half_stamp_size` of 19 pixels. The internal subdivision is the most important parameter in our case. This is because image subtraction assumes flux conservation over the whole field from image to image. For a wide FOV this does not generally hold (due to, for example, differential atmospheric extinction over the field). It becomes necessary to subdivide the field into regions over which the flux conservation assumption holds within the limits set by photon noise/sky background. We empirically find that subdividing into more than 25 sections yields negligible improvement to the standard deviation of the subtracted images (and the light curves of a selected sample of stars) while significantly increasing the computation time.

After obtaining a final reference image (composed of 47 images) for subtraction, we performed subtraction on all the images. At this point we sorted the subtracted images by standard deviation and mean, examining images with large standard deviations and/or means significantly different from zero. This procedure allowed us to identify images with subtle cloud patterns, etc., which might contaminate the photometry. Since image subtraction assumes that the flux of all stars scales by a constant from image to image, any complex background variations/clouds will yield significant residuals over an entire sub-region of the subtracted image. The ease with which very subtle differences in images can be identified is one advantage of using image subtraction over methods to directly measure photometry on original images.

After cleaning, we were left with 800 out of 935 images on which to proceed with photometry.

3.2. Photometry

There are two approaches that one can take toward obtaining light curves and identifying variables with subtracted images. The first is to co-add the subtracted images and search for strong point source signals to identify variable stars for which to obtain light curves. The second is to generate a list of stars from the reference image, measure photometry on the subtracted images for a selection of stars on the list, and scan the resulting light curves for variables. Using the former approach it becomes very difficult to efficiently identify extremely subtle variations, such as those due to a transiting planet, as these tend to get washed out in the overall noise on the image (which includes the co-added Poisson noise of the stars). For this reason we implement the latter

approach. In doing so we do make two sacrifices: any transient phenomena which do not have a signal in the 47 images combined to make the reference image go unnoticed, and constant stars located nearby variable stars will have variable light curves as a result of the weighted aperture photometry performed on the subtracted images by the ISIS routine “phot.csh.” The second problem turns out to be significant for our program, and we describe the steps we have taken to mitigate it in §4.6.

To obtain the list of stars we used the DAOPHOT/ALLSTAR package (Stetson 1987, 1992). The list contains 98,000 objects ranging in magnitude from $I=7.79$ down to 14.87.

We then obtained light curves for all 98,000 objects using the “phot.csh” routine contained in the ISIS package. This procedure first determines a PSF within a region of size `PSF_width` pixels on the reference image using a spline, and then uses the best-fit kernel to transform it into the PSF for the subtracted image. It then measures the flux within a radius of `radphot` pixels from a specified location, weighting it by the PSF, and normalizes by the integral of the PSF squared over a region of radius `rad_aper` pixels. These difference flux measurements can be converted into instrumental magnitude light curves for each object using the flux on the reference image measured by DAOPHOT/ALLSTAR.

In converting from flux to magnitudes it is important to ensure that the flux measured by DAOPHOT/ALLSTAR is properly scaled to the flux measured by ISIS. The DAOPHOT/ALLSTAR fluxes correspond to the flux from PSF fitting using a zero-point of 25.0 magnitudes. In general, this flux is *not* equal to the total number of ADUs in the image contributed by the star in question. For a large aperture radius, the latter value is what is measured by “phot.csh.” To determine the scaling between the two “fluxes” we perform an aperture correction as follows: after fitting a PSF to 98,000 stars in the field, we subtract a number of these stars from the reference image leaving only a sparsely populated image. We then perform aperture photometry on the remaining stars in this sparse image (using a large aperture radius of 7 pixels). Comparing the aperture magnitudes with the PSF magnitudes we find that the PSF magnitudes are consistently brighter by 0.19 mag. We can correct for this difference in scaling by using a zero-point of $25.0 - 0.19 = 24.81$ magnitudes for the DAOPHOT/ALLSTAR reference magnitudes of our program stars.

To optimize the ISIS photometry parameters we ran the “phot.csh” procedure iteratively on a small subset of the 98,000 objects with magnitudes across the entire range. The parameters we varied include (`rad_aper`), the `PSF_width`, and the inner/outer radii of the annulus for measuring the background (`rad1.bg` and `rad2.bg`). We related the parameters so that $PSF_width = 2 * rad_aper + 3$, $rad1_bg = 2 * rad_aper + 1$ and $rad2_bg = 2 * rad_aper + 6$. We also independently varied the radius for photometry (`radphot`) with little effect. We find that when the aperture radius is reduced below 7 for our FWHM of ~ 3 the RMS of the light curves is artificially reduced, while the amplitude of the long period variable light curves decreases and becomes excessively noisy as the magnitude differs substantially from the reference point. We believe that this is the result of performing photometry on only a small portion of the PSF (yielding increased noise)

while simultaneously providing a flux that is not properly scaled (yielding lower amplitudes). For `rad_aper` greater than 7 the effect on the light curves is minimal, with a slight increase in the noise for the dim stars due sampling more of the background. The final set of photometry parameters that we chose include: `rad_aper` = 7, `PSF_width` = 17, `radphot` = 3.0, `rad1_bg` = 15.0 and `rad2_bg` = 20.0.

After obtaining light curves for all the stars in our field, we checked to see if there were any remaining bad frames. To do this we calculated the RMS of each light curve and then calculated, for each frame, the number of light curves for which the magnitude of that frame was more than 3σ from the mean. We identified 12 frames that were consistently “bad” in a large number of light curves. These frames were contaminated by clouds, or airplane tracks, or simply had subtracted images with substantial residuals and background gradients whose cause could not be identified on the original image. After removing these frames from every light curve we were left with a total of 788 contributing frames. Several of the light curves contained an excessive number of outlier points as a result of lying near the edge of the field. To clean these light curves we removed any point with a formal flux error less than 15 ADU as determined by the “phot.csh” routine (the average flux error being ~ 40 ADU for the dimmest stars). Some light curves also contained bad points as a result of lying near a saturated star. Because the profile of saturated stars is not fit by the PSF, these stars yield significant residuals on the subtracted images. Since these residuals change from image to image the contribution of this residual to the aperture of a nearby star changes. For dim stars this effect dominates such that occasionally the difference flux measured by “phot.csh” is more negative than the flux of the star itself as measured by DAOPHOT. These can be eliminated by removing all points with negative infinity magnitude from the light curves. The variability induced by proximity to saturated stars is difficult to distinguish from actual variability, and we will discuss our attempts to deal with this in §4.4.

We used the *Hipparcos* main catalogue (Perryman et al. 1997) to provide the absolute calibration for our instrumental, I-band, reference magnitudes. Using the coordinates we obtained from matching to the Two Micron All Sky Survey (*2MASS*; Skrutskie et al. 1997) as discussed in §3.4, we obtained matches with 55 point sources from *Hipparcos* that also had I-band measurements listed. The I magnitudes listed were all obtained from ground-based measurements, or from transformations of *Hipparcos* measurements in other photometric systems. We find a 1σ uncertainty of ± 0.06 magnitudes on our absolute calibration to *Hipparcos*.

3.3. Photometric Precision

Figure 3 shows the light curve RMS vs. reference magnitude for our 98,000 objects. Because many of the light curves contain outliers that result from non-random errors (e.g. satellite crossings, bad pixels, etc.), before calculating the RMS of Fig 3-A we first sorted each light curve by magnitude and removed two outlier points from each end. From this plot it is clear that we have obtained a photometric precision down to 3.5 millimagnitudes at the bright end. For the dim end the noise

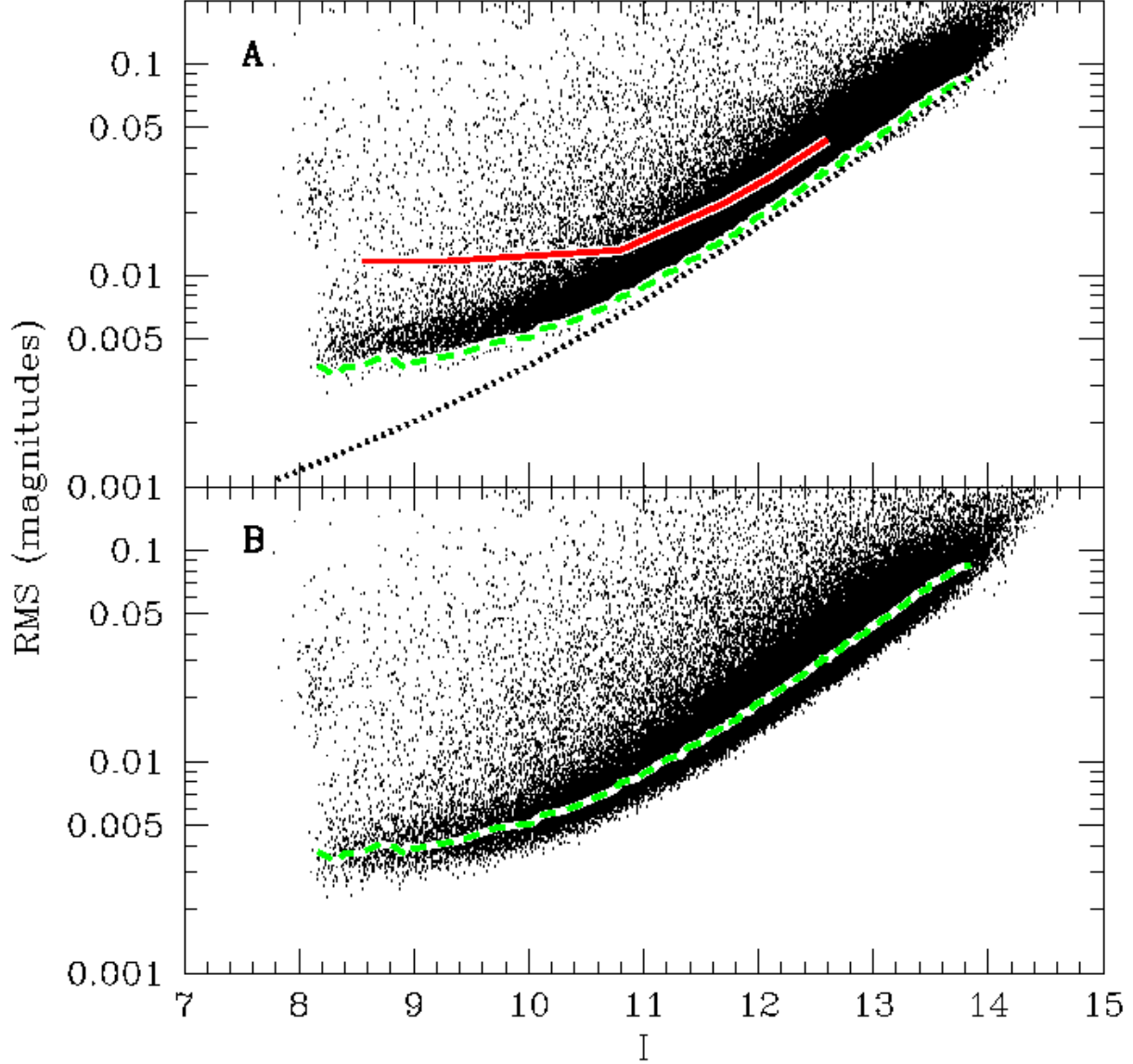


Fig. 3.— (A) RMS vs I -band for the 97,540 lightcurves with $\text{RMS} < 0.2$ mag. The solid line traces the lower envelope for frames exposed without the PSF broadening technique, the dashed one marks the lower envelope of the plotted distribution. The dotted line shows the theoretical limits (photon noise). (B) RMS vs I for the light curves binned by 20 minutes. The dashed line is the same as in (A). The fact that binning reduces the RMS shows that the light curves are not dominated by systematic errors that are correlated on time scales longer than 20 minutes.

is dominated by the background and rises to 0.01 magnitudes at $I \sim 11.3$. This is very close to the results that have been achieved on less dense stellar fields using aperture photometry (see B04). There are a total of 9,004 light curves with RMS better than 10 millimagnitudes, and another 16,540 light curves with RMS between 10 and 20 millimagnitudes.

All of the frames in these light curves were exposed using the PSF broadening technique described in B04. During the same nights images were also obtained without broadening. We performed image subtraction on these “tracking” frames as well, and obtained light curves for a number of objects. In Fig 3-A we graph the outline of the RMS vs. reference magnitude relation for these objects. We see that PSF broadening may improve the precision of the light curves by as much as a factor of 2.8 for the brightest stars even for image subtraction. It should be noted, however, that we did not attempt to optimize the parameters for the narrow PSF. The result that PSF broadening improves the photometric precision when using the ISIS implementation of image subtraction is consistent with what is found in B04 for aperture differential photometry.

Although we achieve very high precision for the brightest stars, it is apparent that we are not photon-limited at the bright end. To determine whether or not our systematic errors are correlated along the light curves, we binned the light curves in time using a bin size of 20 minutes. This reduced the maximum number of points per light curve from 784 to 286, a factor of 2.7. If the errors were correlated on time-scales longer than 20 minutes, this procedure would not affect the RMS of the light curves. But for uncorrelated errors we would expect the RMS to be reduced by 40%. In Fig 3-B we show the resulting sigma vs. reference I diagram, together with a line tracing the bottom envelope from Fig 3-A. At the bright end the RMS approaches 2.5 mmag, or a reduction of 29%, which is consistent with the errors being uncorrelated.

One possible source for our systematic errors is the fact that we are using a front-side illuminated CCD. Random variations across the surface in the optical depth through the gate-structure can result in noise in our photometry since the stars are positioned at different locations on the chip in different exposures. If the starlight is spread over more pixels these variations will tend to average out in each measurement of the magnitude. Because the PSF broadening technique increases the FWHM of the PSF from roughly 1.5 to 3.0 pixels for our observations, it follows that the starlight on the broadened frames is spread over roughly 4 times as many pixels as on the tracking frames. We would expect, then, a reduction by a factor of ~ 2 in the RMS of equally bright stars when using the broadened frames instead of the tracking frames. This is approximately what we see.

3.4. Astrometry

Because the ISIS package provides an image registration routine via “interp.csh”, we do not follow the same steps as B04 to match images to one another. Instead, once we have the X,Y positions of all point sources in our field from DAOPHOT, we use the Delaunay-triangulation

algorithm as described in B04 to match to the *2MASS* catalog. Using the resulting RA/DEC grid for our field, we match our entire list to *2MASS* using a matching radius of $10''$. We then adopt RA/DEC from *2MASS* for the matched sources.

Because *2MASS* contains many objects that are much fainter than our upper magnitude limit, and is at higher resolution than our observations, we only match to *2MASS* sources with $J < 13$. Even at this cut there are over 170,000 *2MASS* sources in the field compared to our 98,000. Taking a cut at fainter magnitude will tend to increase the number of spurious matches between our objects and fainter *2MASS* sources. Although the magnitude that we measure for each “object” will be the summed *I*-band of all objects within roughly $30''$, for the purposes of follow-up we will adopt the convention that our “object” lies at the location of the nearest *2MASS* source within $10''$ that has $J < 13$.

Using a $10''$ matching radius we obtain 83,900 matches, with 6,174 objects having more than one *2MASS* source within $10''$ (multiple matches). For all multiple matches, we choose the closest match as the “real” one. We also matched with smaller radii: for $1''$ there were 16,557 matches, and for $5''$ there were 64,844 matches. To determine whether or not the number of multiple matches is consistent with random matching, we also shifted our entire starlist by $15''$ and by $30''$ and matched it to *2MASS*. For the $15''$ shift we obtained 6776 matches, and for the $30''$ shift we obtained 4103 matches. If the 170,000 *2MASS* objects were randomly distributed across the frame, one would expect to find 1 object for every 24 pixels. Assuming that our 98,000 objects are also randomly distributed we would expect 6,400 random matches between HAT and *2MASS*. This is consistent with the number of multiple matches that we see with the $10''$ matching radius, and with the number of matches that we see with the $15''$ shift. The fact that the number of matches drops as we shift to $30''$ may suggest that the objects are not randomly distributed but have some degree of clustering.

There are a number of objects with $J > 13$ that will not have matches in our catalog. They should account for most of the 14,100 unmatched objects, and indeed 13,101 of these objects have $I > 12$.

4. Selection of Variables

4.1. Rescaling ISIS Errors

Before proceeding with the selection of variables, it is useful to rescale the formal flux errors from ISIS to match the empirically observed errors. This is necessary since the formal errors are assumed to represent the real errors when used by variability tests such as Stetson’s “J” (Stetson 1996). We follow a procedure similar to that used by Kaluzny et al. (1998).

To do this we calculate the reduced chi-square

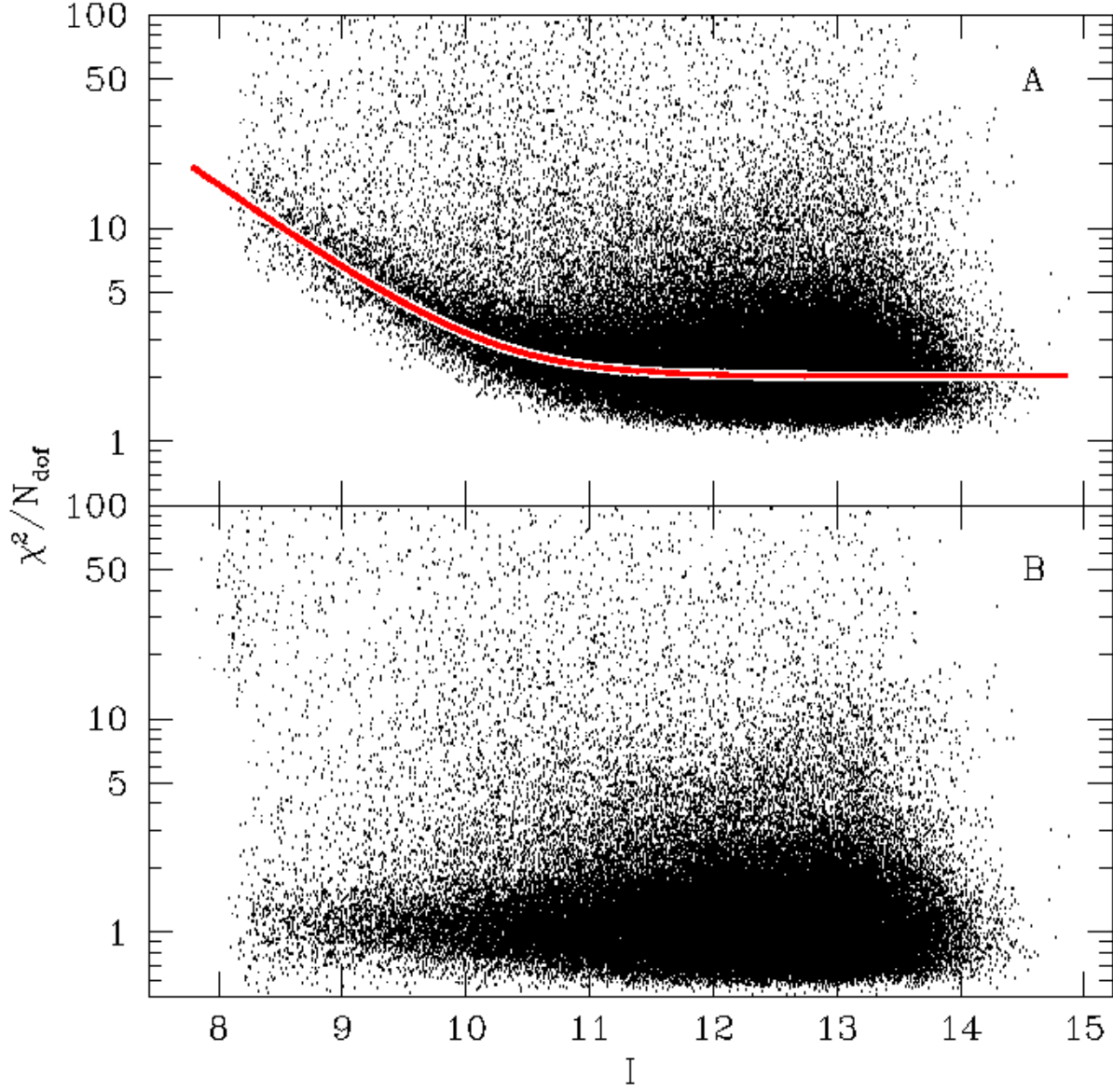


Fig. 4.— (A) Reduced χ^2 of 98,000 light curves vs. I magnitude of the objects on the reference frame. The line shows the function used to rescale the formal photometric errors from ISIS. (B) Reduced χ^2 vs. I following correction of formal flux errors from ISIS (§4.1).

$$(\chi^2/N_{dof}) = \frac{1}{N-1} \sum_{i=1}^N \left(\frac{I_i - \bar{I}}{\sigma_i} \right)^2 \quad (1)$$

for every light curve and plot it as a function of I (Fig. 4). Here I_i is the measured magnitude at time i , \bar{I} is the mean magnitude for the light curve, and σ_i is the formal error assigned to the magnitude measurement. The observed χ^2/N_{dof} rises well above the expected value of 1 at the bright end. This is because systematic errors dominate the light curves of the bright stars as described in §3.3. To account for these systematics in our errors we fit a curve to the “ridge” of the observed χ^2/N_{dof} vs. I distribution. We then multiply the formal errors by the square-root of this function. The resulting “corrected” χ^2/N_{dof} vs. I is shown in Fig. 4-B.

4.2. Stetson’s Variability Index

As a preliminary selection of variable stars, we apply the Stetson “J” variability test (Stetson 1996). The weighting scheme that we use is analogous to the one employed by Kaluzny et al. (1998). We use a time-scale of 30 minutes for pairing, assigning a weight of 1.0 to pairs formed by distinct points, and a weight of 0.1 to “pairs” formed from a single point.

To select the variable stars we apply a cut of $J_s > 1.0$ (Fig. 5). This selects 2830 light curves, all of which show some form of correlated variability.

4.3. Selection of LPVs

The majority of light curves selected with the above procedure do not show any periodicity within the 30 day window of observations. Typically these light curves increase or decrease monotonically over the run, although there are some that achieve a minimum or maximum magnitude. For the purposes of this paper we define a “Long Period Variable” (LPV) to be any variable for which the fit to a parabola is substantially better than the fit to the mean. These are most likely Mira variables or semi-regular/irregular variables.

To separate the LPVs from the other variable stars we apply the following simple cut. We first fit a parabola to all the light curves flagged as variable by the J_s cut. We then calculate the reduced chi-squared, χ_2^2/N_{dof} (χ_2^2 for short), for each fit. True LPVs will show dramatic improvement when fit with a parabola as opposed to fitting with the mean (χ_0^2). We classify any light curve with $\chi_2^2/\chi_0^2 < 0.4$ as an LPV (Fig. 6). This procedure selects 1535 candidate LPVs, leaving 1295 candidate non-LPV variables.

We chose this cut empirically at a point where light curves that may be best fit with a 3rd order polynomial begin to be mixed in with the parabolic light curves. An example of how a light curve with $\chi_2^2/\chi_0^2 \ll 0.4$ compares to a light curve with $\chi_2^2/\chi_0^2 \lesssim 0.4$ is shown in the inset of Fig. 6.

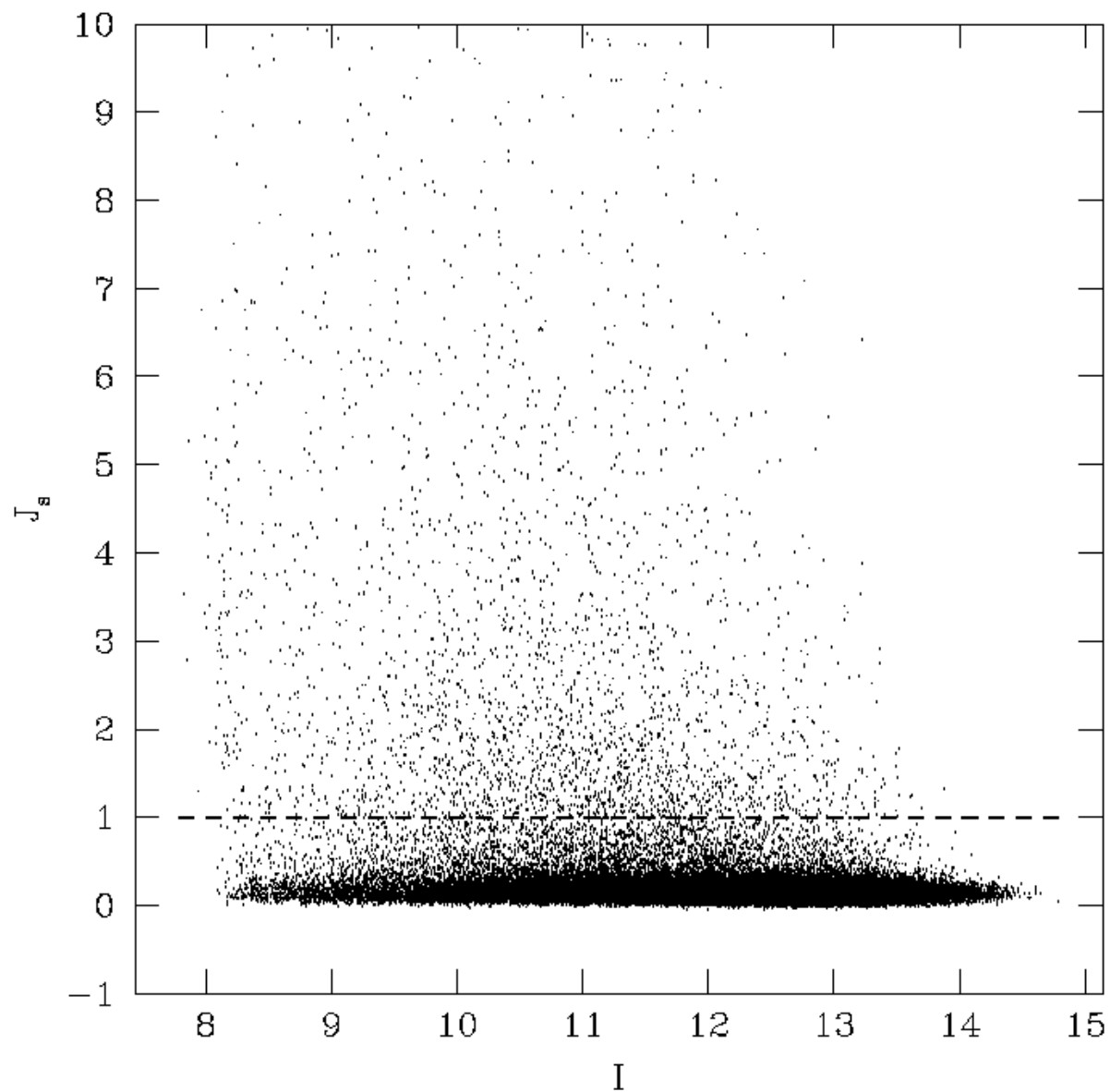


Fig. 5.— Plot of Stetson’s “J” variability index (J_s) vs I magnitude. The 2830 objects lying above the dashed line ($J_s = 1.0$) were selected as candidate variable stars (§4.2).

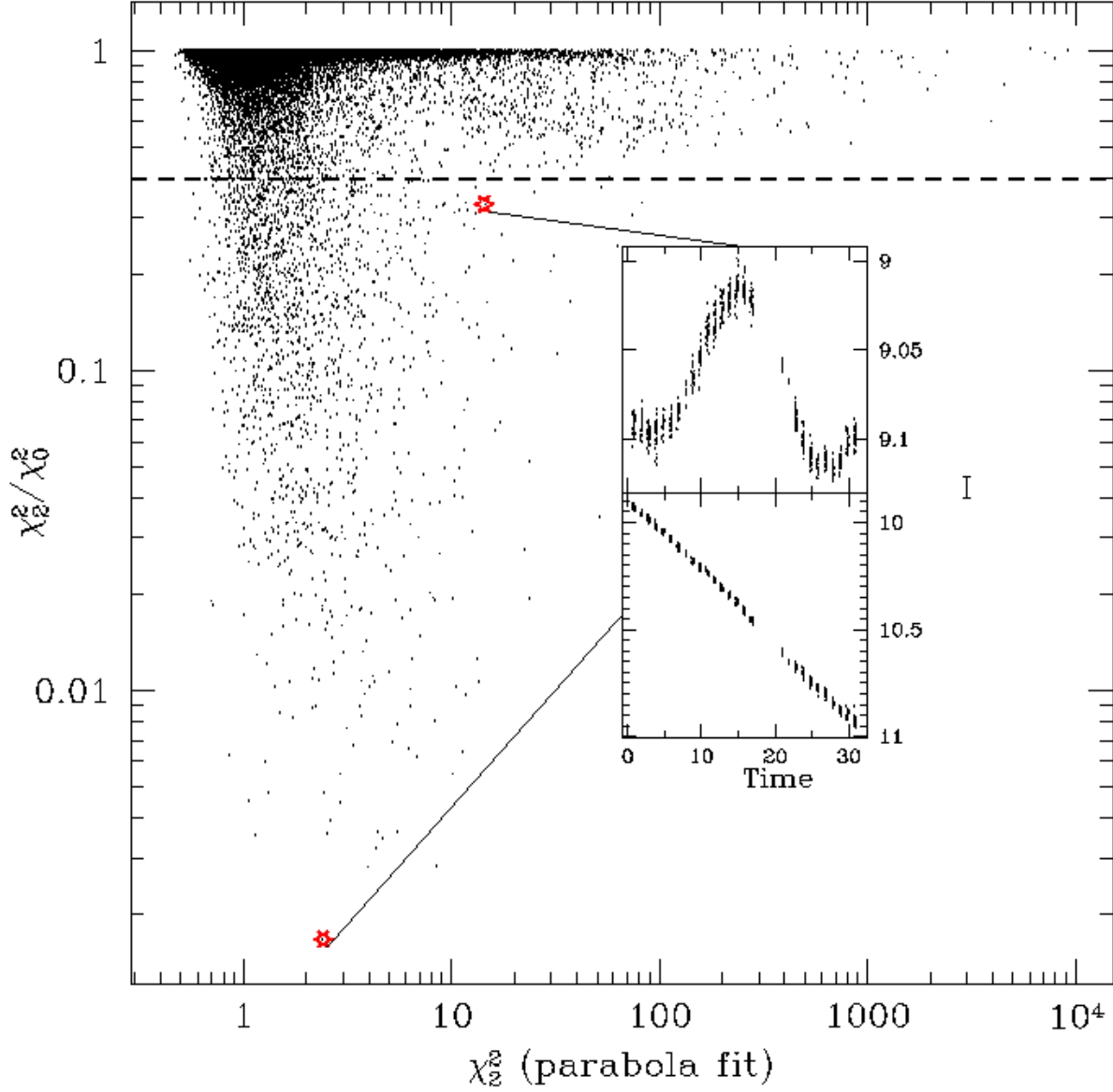


Fig. 6.— Ratio of reduced chi-square for fit of parabola to reduced chi-square about the mean (χ_2^2/χ_0^2) vs reduced chi-square for fit of parabola χ_2^2 . This plot is for all 98,000 light curves. The 1535 objects below the dashed line ($\chi_2^2/\chi_0^2 = 0.4$) that also had $J_s > 1.0$ are light curves that we classified as LPVs (§4.3). (Inset) Light curves with $\chi_2^2/\chi_0^2 \ll 0.4$ are better fit with a parabola than those with $\chi_2^2/\chi_0^2 \lesssim 0.4$.

4.4. Removal of Spurious Variables

In §3.3 we claimed that our systematic errors are uncorrelated on time-scales longer than 20 minutes. Although this is true for the majority of stars, we do see a number of light curves that show nearly identical variations. These trends can be classified into three basic types: template1-like (Fig 7-A), template2-like (Fig 7-B), and template3-like (Fig 7-C). Since image subtraction assumes conservation of flux, there are a number of light curves that show the same trends, but reflected about the horizontal axis. A plot of the X,Y coordinates of template1-like objects reveals that many of them lie near saturated points. The relatively large apertures used in “phot.csh” likely sample some of the residual flux of a nearby saturated star on a subtracted image (§3.2). As the background changes the percentage of this flux that ISIS attributes to the star similarly changes. The result is a light curve that traces the general variation in the background of the images. We believe there is a similar culprit for the template2-like light curves, as template2 resembles a scaled inverse of template1. Another possible source for the trends between HJD-2806 and HJD-2815 is the lack of separate flat-fields for those nights. Because flat-fields were missing for those nights we reduced the data with flat-fields from neighboring nights (2806-2810 used 2805 and 2811-2815 used 2816). We also observed a number of light curves that appeared to be correlated with the airmass of the observations. These tended to be removed more efficiently by fitting to template1 or template2 than by defining a separate template, as a number of “true” variables showed small 1 day oscillations on top of an over-all “real” variation, and would be rejected by a separate template. We also noticed a number of LPVs that had light curves that almost exactly traced template3 (this was after the blending correction of §4.6). If one were to smooth out the kink between HJD-2810 and HJD-2815 in template3, then the peak in the light curve would be near HJD-2820, at the time of new moon. We suspect that this trend may result from a change in background that correlates with the phase of the moon, and would typically corrupt saturated stars, or objects near saturated stars. However, it should be noted that the moon was full on HJD-2805, so template3 does not appear to trace the lunar phase prior to that date.

Regardless of the nature of these systematic variations, we believe the most straightforward way to reject light curves that show these trends is to reject those that have a substantially smaller chi-squared when fit, point-by-point, to the template light curves, than when fit to the mean. When fitting to the templates we allow one free parameter: an overall scaling of the variations above and below the mean. We apply different cuts for the LPV and non-LPV light curves, since a very strict cut tends to reject more LPVs than non-LPVs, particularly for fitting to template1. For template3 we also imposed a magnitude cut to avoid removing variables that had a numerically good fit, but had a maximum at a different time and were thus probably not spurious. Looking back through the permitted LPVs we rejected 4 candidates by eye that showed a strong resemblance to template3 or template2. The template3 cut was applied after all other cleaning steps.

As a check on our template3 rejections we examined the light curves released by the Northern Sky Variability Survey (NSVS, Wozniak et al. 2004) for the 13 objects rejected by template3. The survey made use of the Robotic Optical Transient Search Experiment (ROTSE-I) to provide to

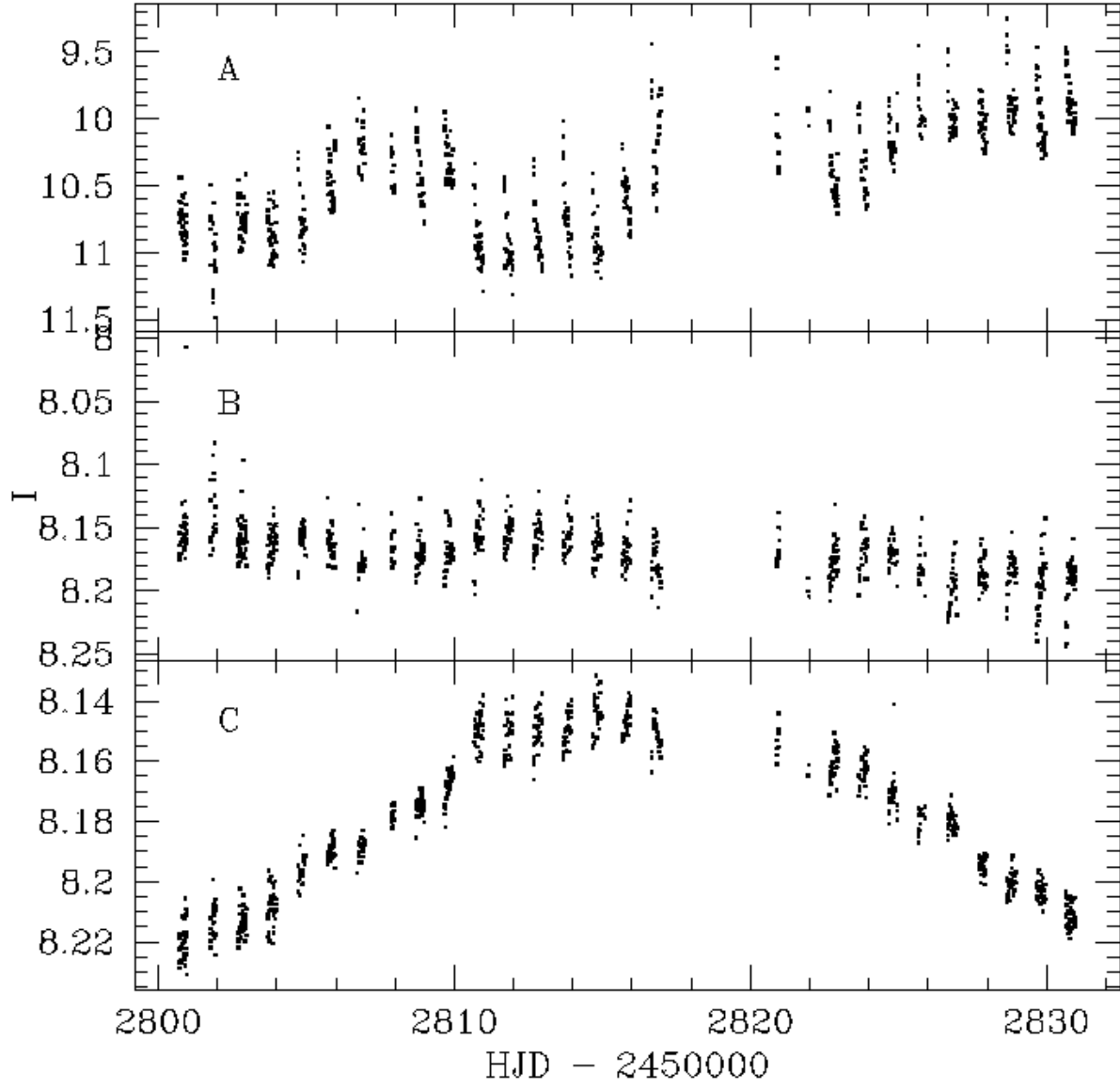


Fig. 7.— Light curves used as templates to remove spurious variables (§4.4).

the public a temporal record of the northern sky over the optical magnitude range from 8 to 15.5. Notably the optics and CCD used for this telescope are now in use on the HAT-5 instrument. The majority of our template3-like light curves have a full-amplitude of ~ 0.05 mag, however as they are classified as LPVs, one might expect that if they are real then a number of them should have full-amplitudes greater than ~ 0.1 mag when observed over a longer baseline. The typical RMS for the NSVS light curves of these objects is ~ 0.05 mag, so any variations with full-amplitude less than ~ 0.1 mag would be unrecognizable in these light curves. We find that 3 of the template3-like light curves appear to show variations in the NSVS. These 3, including HAT199-648, HAT199-3997 and HAT199-4205 will remain in our catalog. It should be noted that all three of these light curves show an inverted template3-like shape, and that 3 of them have full-amplitudes greater than 0.1 magnitudes in our observations, and are therefore already suspect as template3-like.

For the variables classified as LPVs we reject 9 light curves with $\chi^2_{temp1}/\chi^2_0 < 0.35$, 10 light curves with both $\chi^2_{temp3}/\chi^2_0 < 0.23$ and $I_{ref} < 10.0$, and an additional 4 by eye. For non-LPVs we reject 359 light curves with $\chi^2_{temp1}/\chi^2_0 < 0.6$ and another 99 light curves with $\chi^2_{temp2}/\chi^2_0 < 0.85$.

As a further cleaning step we also rejected 46 of the non-LPV light curves that had fewer than 693 points. We did not reject 2 light curves that had fewer than 693 points but appeared to show real variability.

4.5. Selection of Periodic Variables

To search the remaining 791 candidate non-LPV variable stars for periodicity, we use a variation of the period finding algorithm by Schwarzenberg-Czerny (1996). This algorithm is implemented in a code due to J. Devor (private communication). The codes provides the two “optimal” periods, along with a measure of confidence for these periods (σ_{AoV}).

Using the best period as a starting point, we proceeded to classify the remaining 791 non-LPV light curves by hand as either periodic (with period less than 14 days), miscellaneous (a light curve that is not an LPV, and does not have a period < 14 days) or a light curve to reject (typically light curves that appeared to be dominated by periods that were harmonics of one day, or light curves that resembled the trends of §4.4). We chose a 14 day cut-off for the period to ensure that any light curve we classified as periodic completed more than 2 full periods within the window of observations. Since rejecting light curves by eye is a highly subjective procedure we decided to find objective cuts that would generally yield the same subjective classifications. We rejected light curves whose best period fell near a harmonic of one day and had a low value of σ_{AoV} , or light curves with a best period greater than 8 days and $\sigma_{AoV} < 5$. For the remaining light curves we called the object “periodic” if the best period was less than 14 days, and “miscellaneous” if not. These particular cuts were chosen empirically as providing the cleanest removal of “suspicious” light curves. The results of these cuts are shown in Figure 8. We looked through the rejected light curves and rescued 8 cases that we believed were clearly variables. We also looked through the periodic

and miscellaneous light curves, rejecting 5 light curves that showed a significant resemblance to one of the templates (§4.4). There were 294 light curves rejected in this step. We erred on the side of caution for the rejection cuts, a look through the rejected light curves reveals many other probable “true” variables. For this reason we do not claim completeness for our periodic or miscellaneous class variables.

4.6. Blending

Following the above classification/cleaning procedures, and prior to the removal of the template3-like light curves, we were left with 3 sets of variable stars: 1526 LPVs, 266 miscellaneous variables, and 231 periodic variables. However, as mentioned in §3.2, one short-coming of the ISIS photometry program “phot.csh” is that it does not account for blending in the subtracted images. Although true variables are generally well separated in the subtracted images, any given variable may have a number of non-variable stars within a `rad_aper`. As a result, “phot.csh” will sample a portion of the variable flux from the nearby variable star when measuring the magnitude of the non-variable star, and our procedure may flag some of these stars as variables. Since “phot.csh” weights each pixel in the aperture by the PSF, “phot.csh” will measure less flux for the non-variable stars than for the true variables, as the non-variables will be off-center from the variable flux. This suggests a method to separate the true variables from the blended light curves.

The first step is to identify blending groups. From each blending group we identify the true variable as the light curve that has the highest standard deviation (in flux). To select the blending groups we first find all pairs of variable stars that are separated by fewer than 6 pixels. There are a total of 461 pairs (well above the expected number due to random matching) involving 695 distinct light curves. We then form groups so that pairs like 1-2 and 2-3 will be grouped into 1-2-3 etc. The largest groups contained 5 light curves (there were 3 of these groups). This formed 305 groups so that 390 objects were rejected as blended light curves. Two of the remaining periodic variables were then removed by hand as they showed no obvious periodicity, and a strong likeness to template1.

Following the correction for blending (and removal of template3-like LPVs as per §4.4) we arrived at our final list of variables consisting of 1169 LPVs, 241 miscellaneous variables and 207 periodic variables for a total of 1617 distinct variables. The periodic variables were then classified, by hand, into two general classes: eclipsing variables (157 objects) and pulsating variables (50 objects). These further classifications are subjective and represent the authors’ suspicions as to whether or not the light curve appears to show some form of eclipses.

Because we only choose one true variable from each blending group we will reject true variables that lie within 6 pixels of other, larger amplitude (in flux), true variables. When two true variables are nearby one another, the light curves of both objects will likely show variability blending. Our procedure will reject the true variable whose flux light curve has a smaller standard deviation.

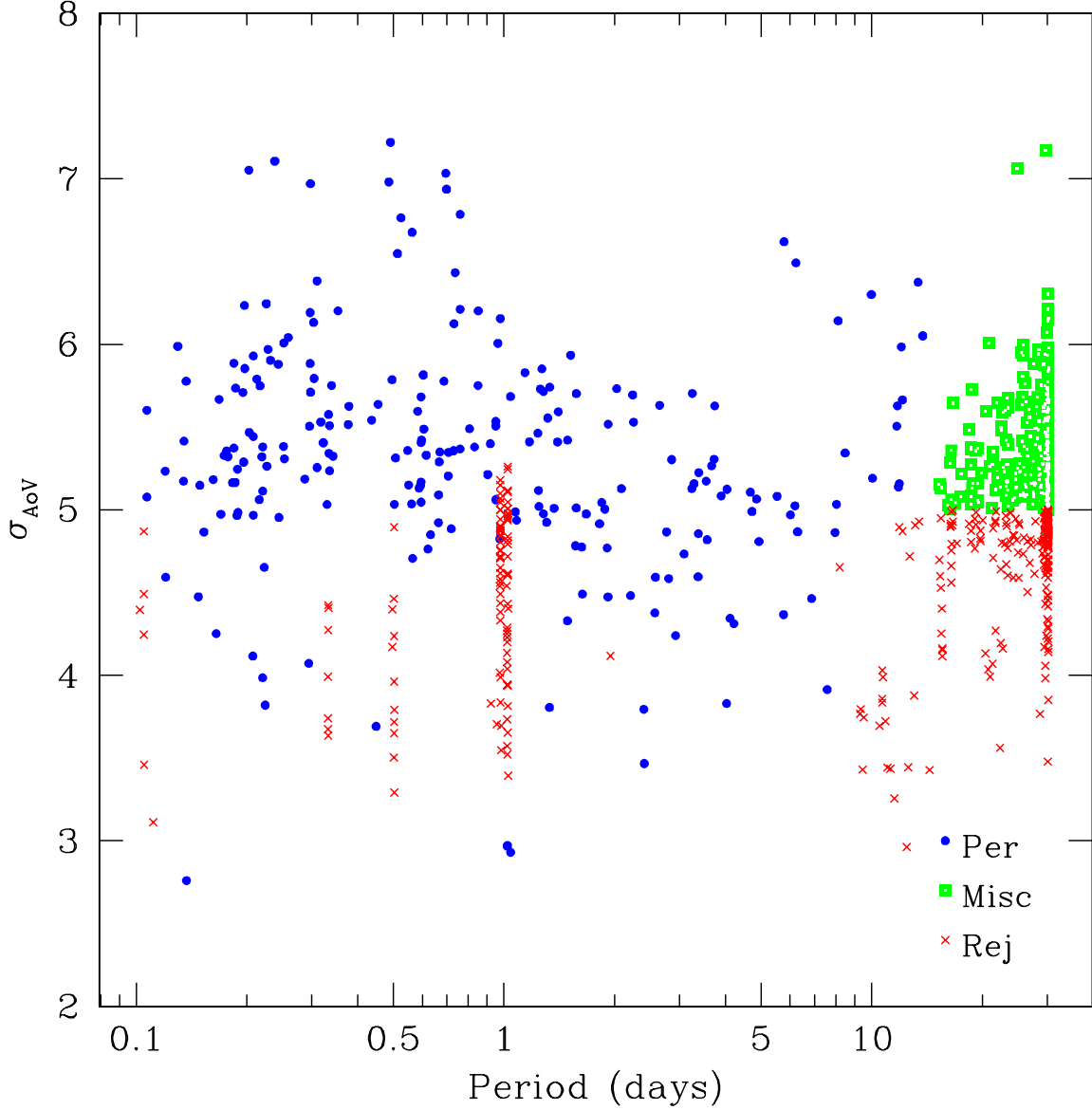


Fig. 8.— Period vs σ_{AoV} for the remaining 791 non-LPV variables. σ_{AoV} is the measure of confidence assigned to the period fit (see §4.5). The dots show the 231 objects classified as “periodic”, the boxes are the 266 objects classified as “miscellaneous” and the x’s are the 294 rejected light curves. Periodic light curves have periods less than 14 days and do not (except in a few cases) have periods near a harmonic of one day. Miscellaneous light curves have $P > 14$ days and $\sigma_{AoV} > 5$.

However, the light curve of the accepted variable will likely show some variations due to the rejected variable. For 1617 variables randomly distributed across the image, we expect ~ 70 such pairings, or roughly 4% of all cases. Since we are more inclined toward correctly identifying variables than forming a complete list (that will include many false-positives) we choose to live with the rejections. It should be noted, however, that as many as 4% of our variable star light curves may show contamination from another nearby variable star which is not included in the list. This number may be even higher if there is clustering as suggested in §3.4.

As an example of this variability blending consider Figure 9. Figure 9-A shows the light curve of an object that we matched with V484 Cyg, an EA/SD binary with eclipses of 1 mag in V (between 13.5 and 14.5) and a period of 1.29 days, as well as to V1360 Cyg, a known Mira variable. Our observations reveal a monotonic decrease in flux from $I = 9.48$ to $I = 10.11$ over 30 days, with slight eclipses. A search of nearby objects revealed a star within 2 pixels with a light curve that showed deeper eclipses on top of an overall declining envelope (Fig 9-B). Indeed both these objects are matched to separate *2MASS* objects. This, we believe, is an especially pronounced case of variability blending where two real variables lie within each others’ aperture and hence the variability is blended into both objects. In this case Fig 9-B likely corresponds to V484 Cyg, and Fig 9-A to V1360 Cyg. Our selection method retained V1360 Cyg while rejecting V484 Cyg as a blended light curve. Because the light curve of V484 Cyg is strongly corrupted by the presence of the nearby LPV, we will not attempt to “rescue” it into the catalog, and will only include V1360 Cyg.

It is important to stress that in this procedure we do not, in any way, correct for the blending that results from resolution limits whereby a number of distinct sources are blended into an individual object. Indeed many of the individual light curves may consist of the summed light from several sources lying along the same line of sight. Instead, the blending that we correct for is the blending of variability into multiple resolved objects that results from “phot.csh” applying simple weighted-aperture photometry on the subtracted images.

5. Catalog of Variables

The full catalog of variable stars, including *2MASS* coordinates and IDs where available, will be available with the electronic version of the refereed paper. The catalog and light curves are also available on the world-wide-web⁴. For illustration we display the first 9 rows of the catalog in Table 1 and Table 2. In the table we provide the HAT-ID for each object, which uses the form HAT199-?????, where the number is between 00001 and 98000 and sorts the light curves by reference magnitude. In this section we discuss the overall properties of the various classes of variables, as well as some of the interesting cases from each class.

⁴<http://cfa-www.harvard.edu/gbakos/HAT/LC/199/>

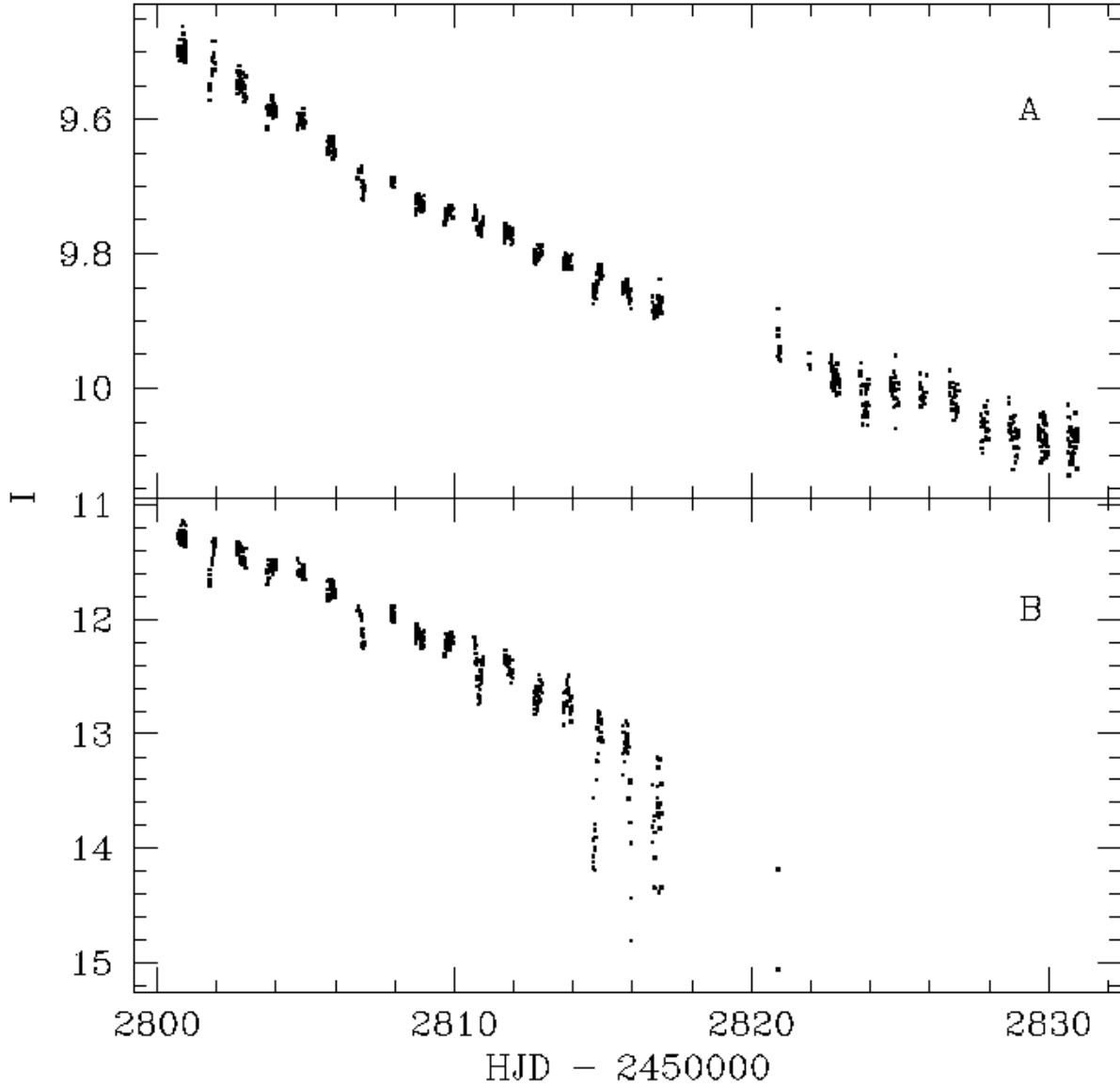


Fig. 9.— (A) LPV matched to V484 Cyg, an EA/SD binary, as well as to V1360 Cyg, a Mira variable. The eclipses are less pronounced than in (B), meaning that this light curve likely corresponds to the Mira V1360 Cyg. (B) Light curve of an object within 2 pixels of (A). This light curve shows deeper eclipses than (A) and is likely V484 Cyg. The larger flux variations due to (A) are blended into this light curve. V484 Cyg is not included in the catalog of variables.

5.1. Matching to Known Variables

To cross-check with known sources, we matched our list of variables to the Combined General Catalog of Variable Stars (*GCVS*, Kholopov et al. 1998). The *GCVS* contains 310 objects in our field; we obtained matches to 128 of these using a $30''$ matching radius. As mentioned above, one of our sources matched to two independent *GCVS* sources, so that only 127 of our sources were known. To match we used *2MASS* coordinates for our objects where available, and used the J2000 coordinates from SIMBAD for the *GCVS* objects. 82 of the matches lie within $5''$, we take a liberal matching radius $30''$ to allow for matches to variables that do not have *2MASS* coordinates, as well as to allow for the possibility that some of our variables are matched to the incorrect *2MASS* counterpart.

Of the 182 *GCVS* variables that do not match with one of our variables, 122 of these have $V > 13.5$ and are thus likely to either be too faint to detect as stars, or so faint that the variations are lost in the background noise in our observations. There are 20 unmatched variables with $V < 10$ which could be saturated in our I-band observations. Of the remaining 40, there are 13 EBs, 9 of which are EA, which could go undetected if none of the eclipses are observed, or if only small portions of a few eclipses are observed. There are 7 Miras that have very long periods ($> 280\text{d}$) for which the change in magnitude over 30 days may have been too small to detect. And there are 13 semi-regular and slow irregular variables, all of which may have only varied slightly over the course of our observation. Finally we can expect ~ 5 *GCVS* variables to be excluded from the catalog due to variability blending. We see that we can account for all of the *GCVS* variables in our field to which we did not obtain matches.

There have also been some more recent searches for variability in fields overlapping this one. Notably Alonso et al. (2003), as part of the STARE project, found that over 40 of the ~ 14000 stars observed in their Cyg0 field had pulsation periods between 5 and 40 days. Of these they identify HD227269 as a highly eccentric eclipsing binary showing possible pulsations. We do detect HD227269 as an eclipsing binary, and also see the same pulsations (Fig. 10). Alonso et al. mention, however, that a DSS image of the star reveals a companion that is similar in brightness within $\sim 9''$. At this separation the stars would be blended in our observations, and it is possible that the pulsations are not occurring in the binary system, though this system does merit further investigation.

Another transit search that we overlap with is the Vulcan Photometer project which has found over 50 eclipsing binaries out of 6000 stars observed (Borucki et al. 2001). Of the brightest 6000 stars we observed, 24 were eclipsing binaries. However, because our brightest stars may contain many more blended objects than the 6000 relatively isolated stars observed by Vulcan, these two populations may not be directly comparable. The differences in the detection rates may also be partially explained by differences in classifications. We should also note that the Vulcan binaries include many low-amplitude systems which may not have $J_s > 1$ and hence would not be flagged as “large-amplitude” variables by our method.

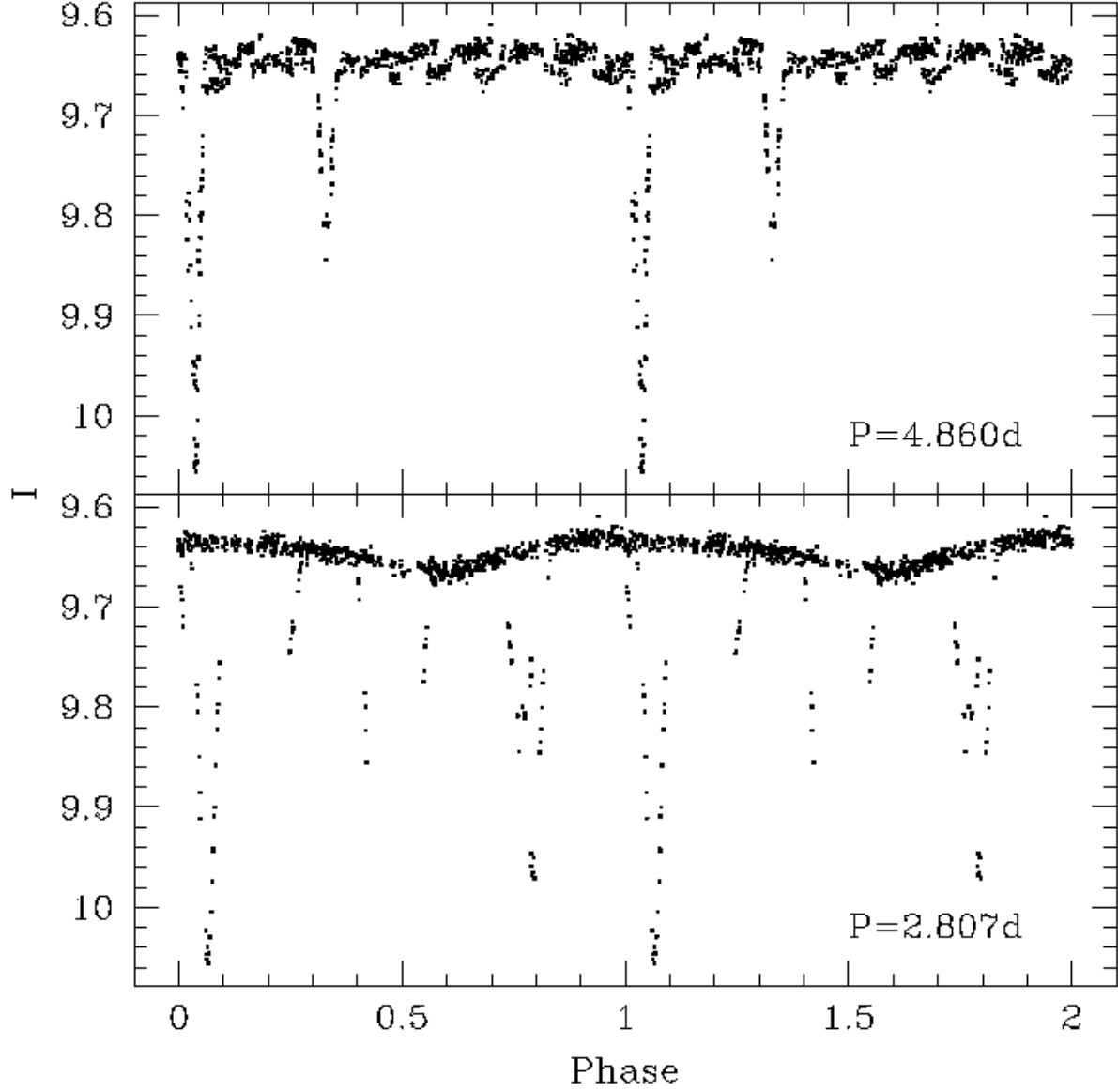


Fig. 10.— Phase folded light curve of HD227269 shows eclipses with a period of 4.860 days and pulsations with a period of 2.807 days. The system may be a blend between two distinct variables separated by $\sim 9''$ (§5.1).

In §4.4 we made use of the NSVS light curve database (Wozniak et al. 2004) to manually check the rejected template3-like light curves to determine if any of these showed variability in an independent experiment. It may be useful in the future to also compare our entire catalog of variables with the NSVS database, however that is beyond the scope of this paper.

5.2. Long Period Variables

As mentioned in §4.3, we cataloged any object whose light curve was well-fit by a 2nd order polynomial as an LPV. We identified 1169 LPVs, of which 1072 are newly discovered variables. Figure 11 shows a few of the interesting cases.

The majority of the LPVs are likely to be Mira variables which all have periods longer than our 30 day window. Indeed 77 of the 97 matched LPVs are known Miras. Recently there has been a great deal of interest in pinning down the various P-L relations for Miras observed by the microlensing surveys (e.g. Wood et al. 1999, Wood 2000, and most recently Groenewegen 2004). All of these have used observations of the Large and Small Magellanic Clouds where the distances can be factored out of the relations. Because we cannot assume a uniform distance for our observations, this population of Miras will likely be less useful towards this endeavor. Our population, however, is substantially brighter and hence may be more useful for detailed investigations of AGB stars.

Figure 12 shows the location of the LPVs on a J vs. J-K color magnitude diagram (CMD). The infrared magnitudes J, and K are taken from the match to *2MASS*. As expected the LPVs are generally redder than the majority of stars, and tend to lie along the giant branch of the CMD.

Among the more exotic variables that we classify as LPVs are V1016 Cyg, a well-studied symbiotic nova whose cool component is a $P = 474$ day Mira (e.g. see Parimucha 2003), and a few RV Tau stars including GK Cyg, and V967 Cyg.

5.3. Periodic Variables

We identified 207 large amplitude (full amplitude greater than 0.032 mag) variables that show periods less than 14 days; 180 of these are newly discovered. As discussed in §4.5 this cutoff at 14 days was to ensure that any star classified as periodic had been observed for two full periods. We further classified the periodic light curves into 157 eclipsing binary-like (EB) light curves, and 50 pulsating variable-like light curves. Figure 13 shows light curves for 48 of the EBs, and Figure 14 shows 48 of the pulsating variables (the other two pulsating variables are shown in Figure 17).

Of the 26 periodic variables matched to *GCVS* objects, 10 are Algol type EBs, 2 are β Lyr type EBs, 3 are WUMa type EBs, 3 are Cepheids, 1 is a population II Cepheid, and 4 are RR Lyr variables. The other known periodic variable which has no counterpart in the *GCVS* is HD227269 (see §5.1).

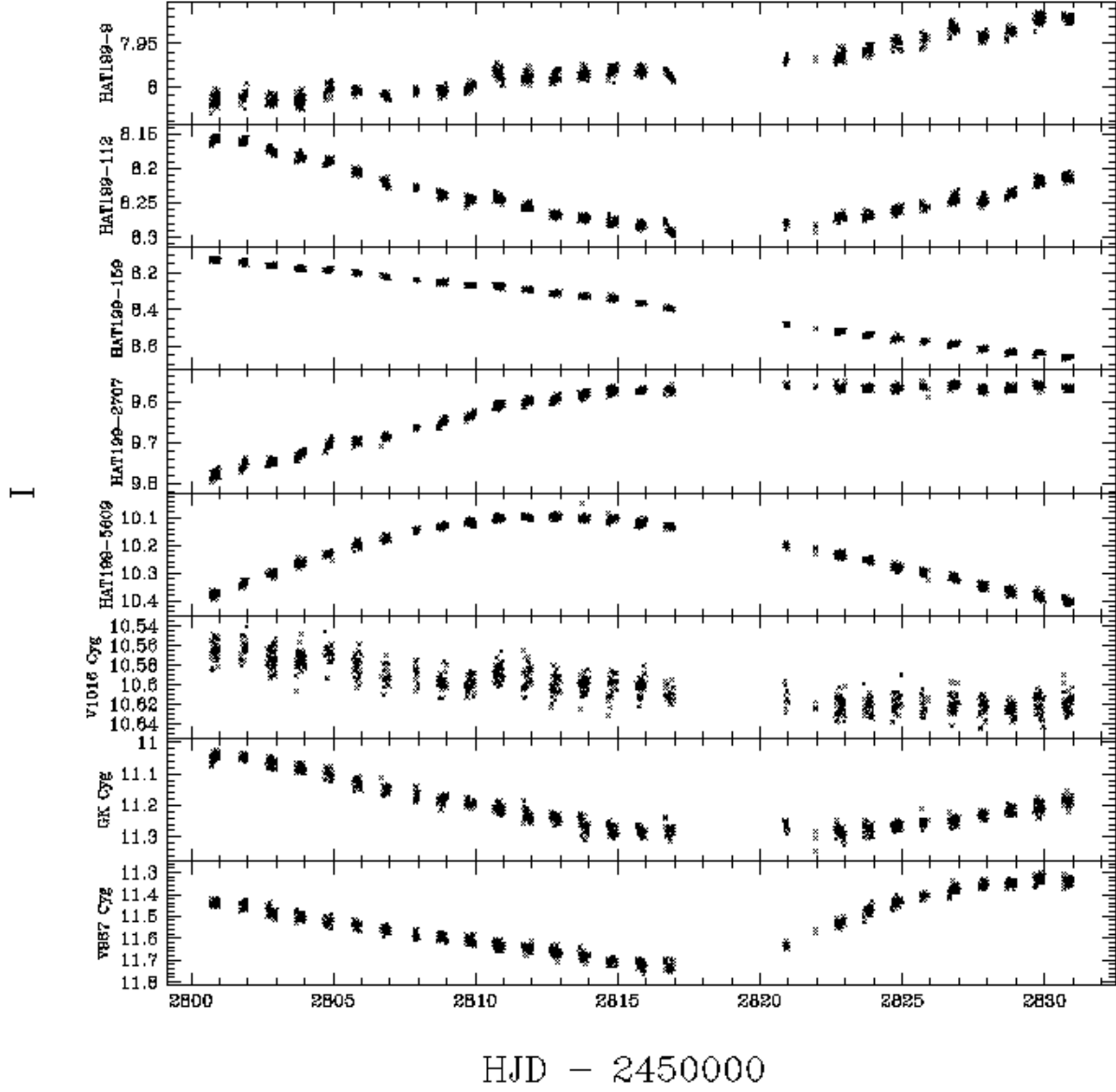


Fig. 11.— I-band light curves of 8 LPVs in our catalog. A few of the variables that matched with the *GCVS* include: V1016 Cyg, a symbiotic nova, and GK Cyg and V967 Cyg which are RV Tau variables.

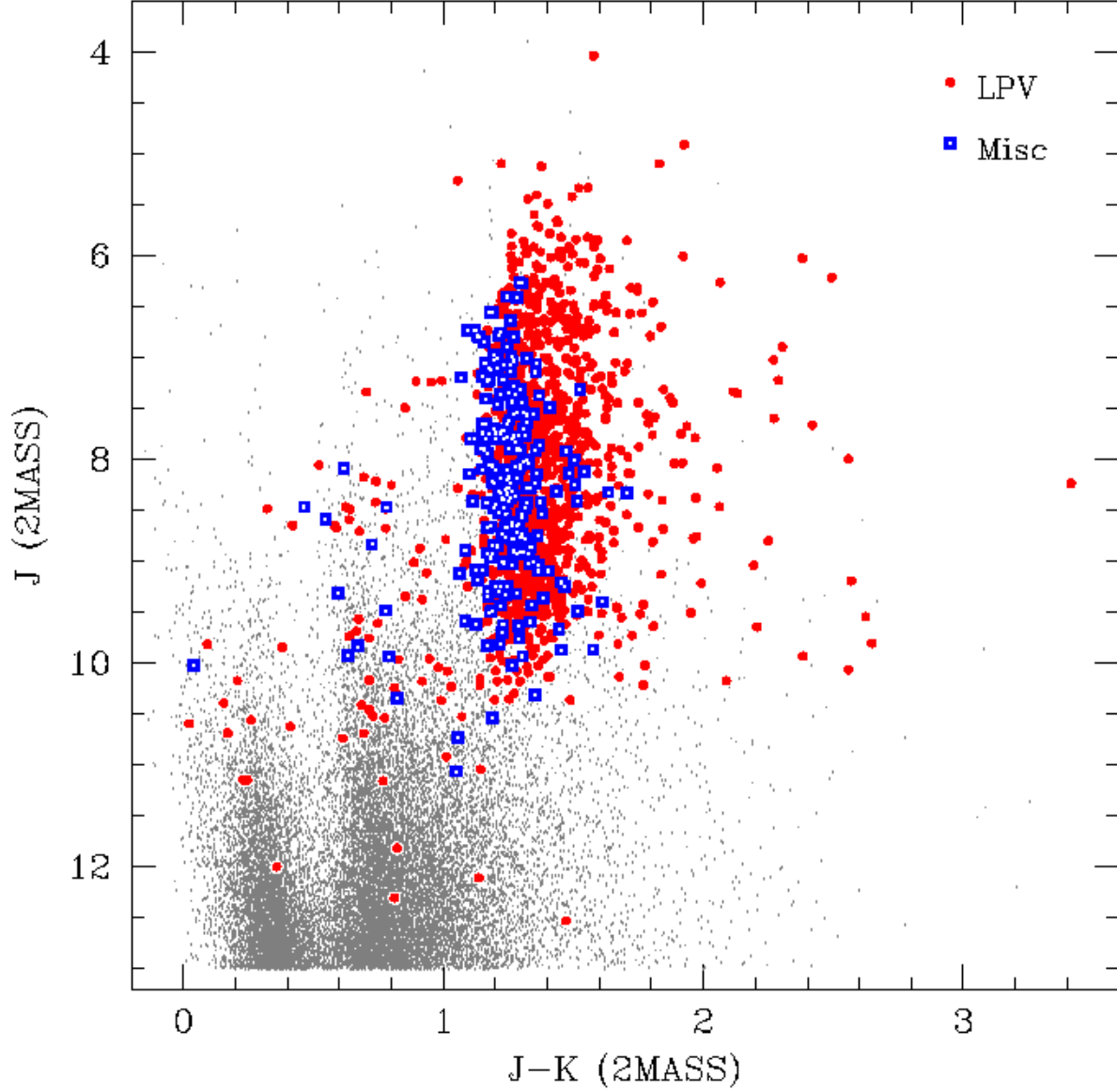


Fig. 12.— J vs. J-K CMD showing location of LPVs and miscellaneous variables relative to one tenth of the *2MASS* objects in our field with $J < 13$. Magnitudes are taken from *2MASS*. LPVs are shown as dots, miscellaneous variables as boxes, and the general population of objects is shown in grey. Note that both the LPVs and miscellaneous variables are generally redder than the overall population with LPVs being typically redder than miscellaneous variables. LPVs are mainly Mira variables, while miscellaneous may include many type I and type II Cepheids that have periods between 14 and 30 days. The bluest miscellaneous variable, with $J = 10.02$ and $J - K = 0.039$ is V1920 Cyg, a PV Tel type variable (§5.4).

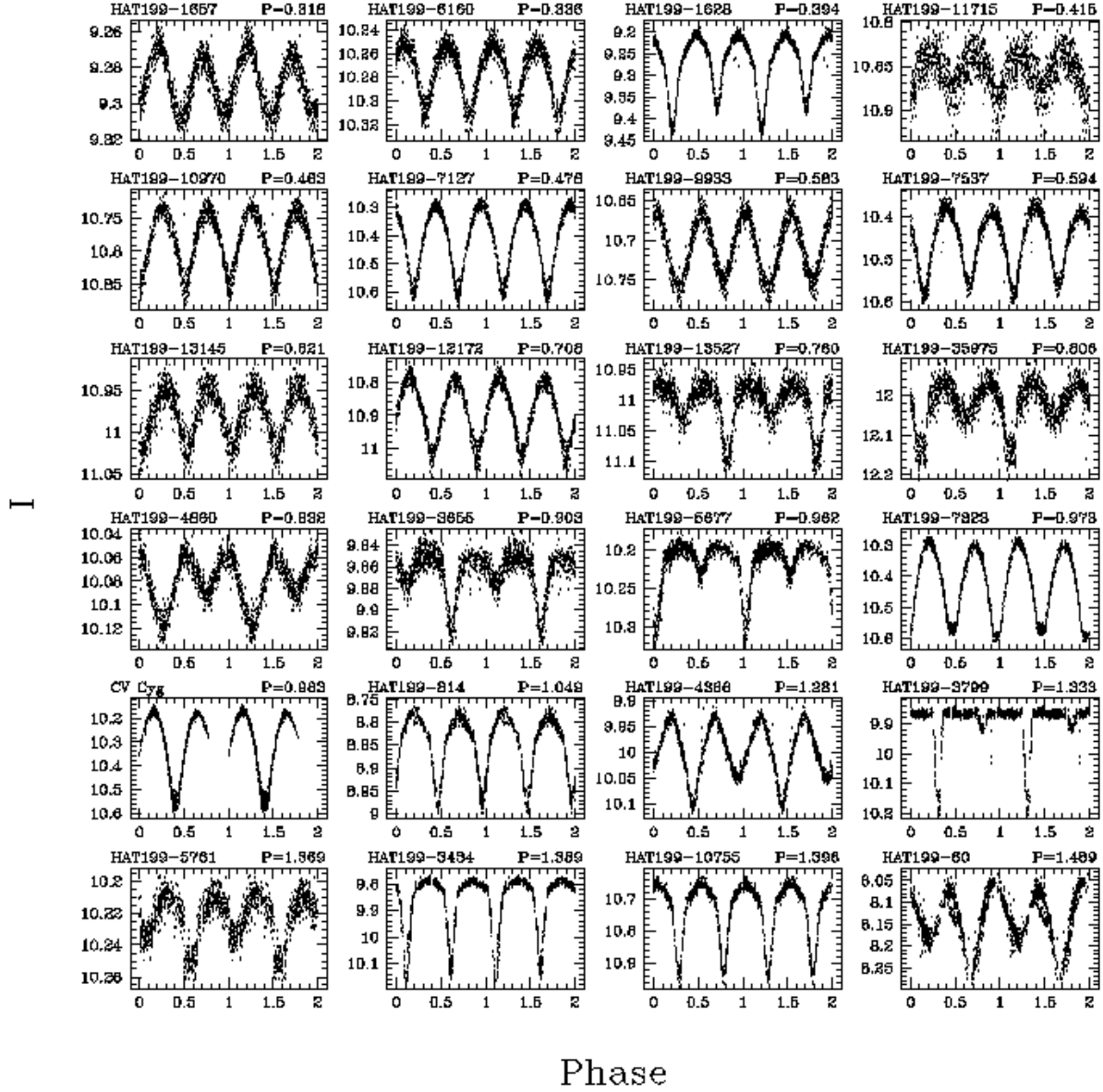


Fig. 13.— I-band light curves, sorted by period (given in days), for 48 of the 157 EBs in our catalog. *GCVS* names are provided where available.

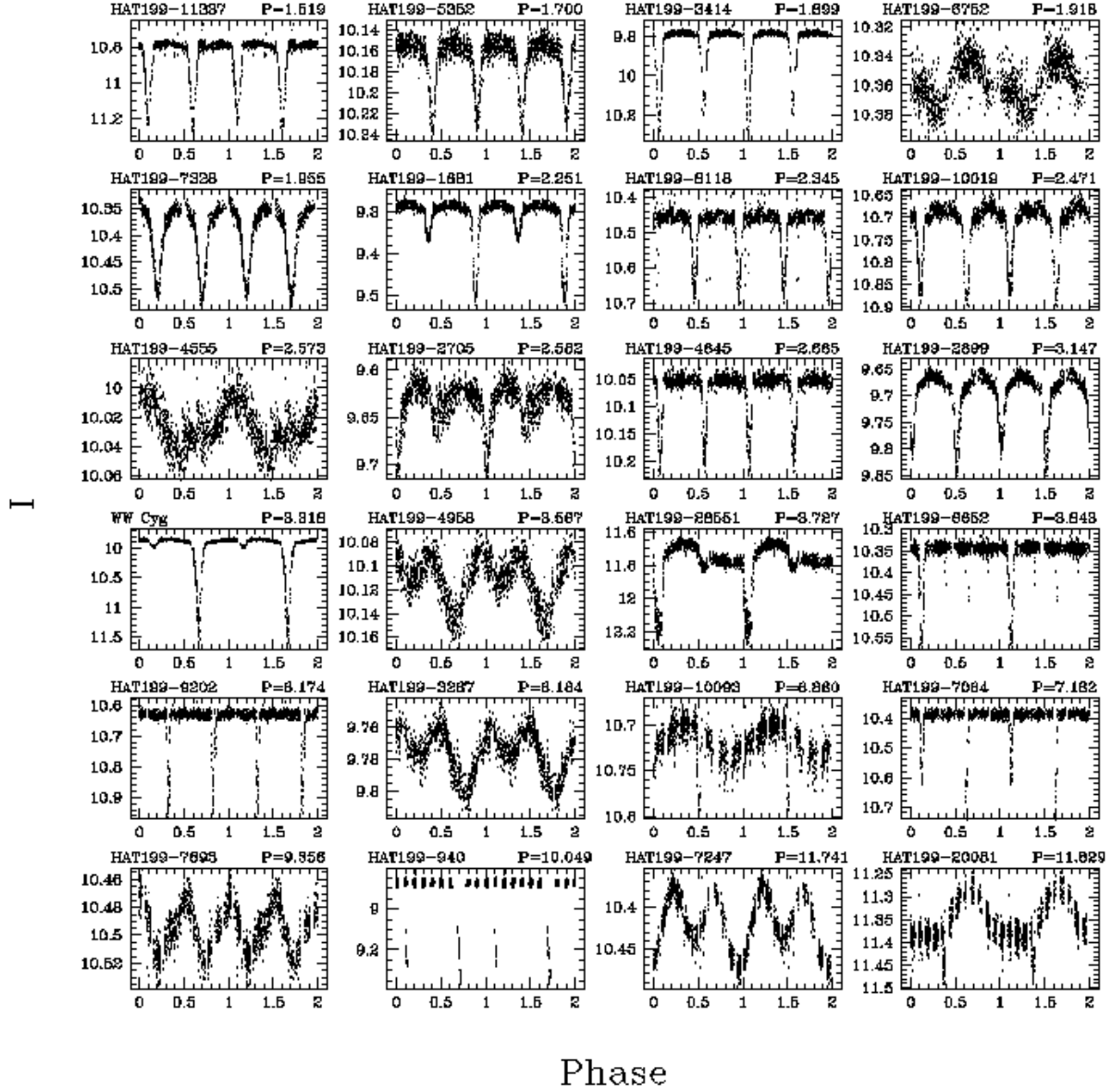


Fig. 13.— *Continued.*

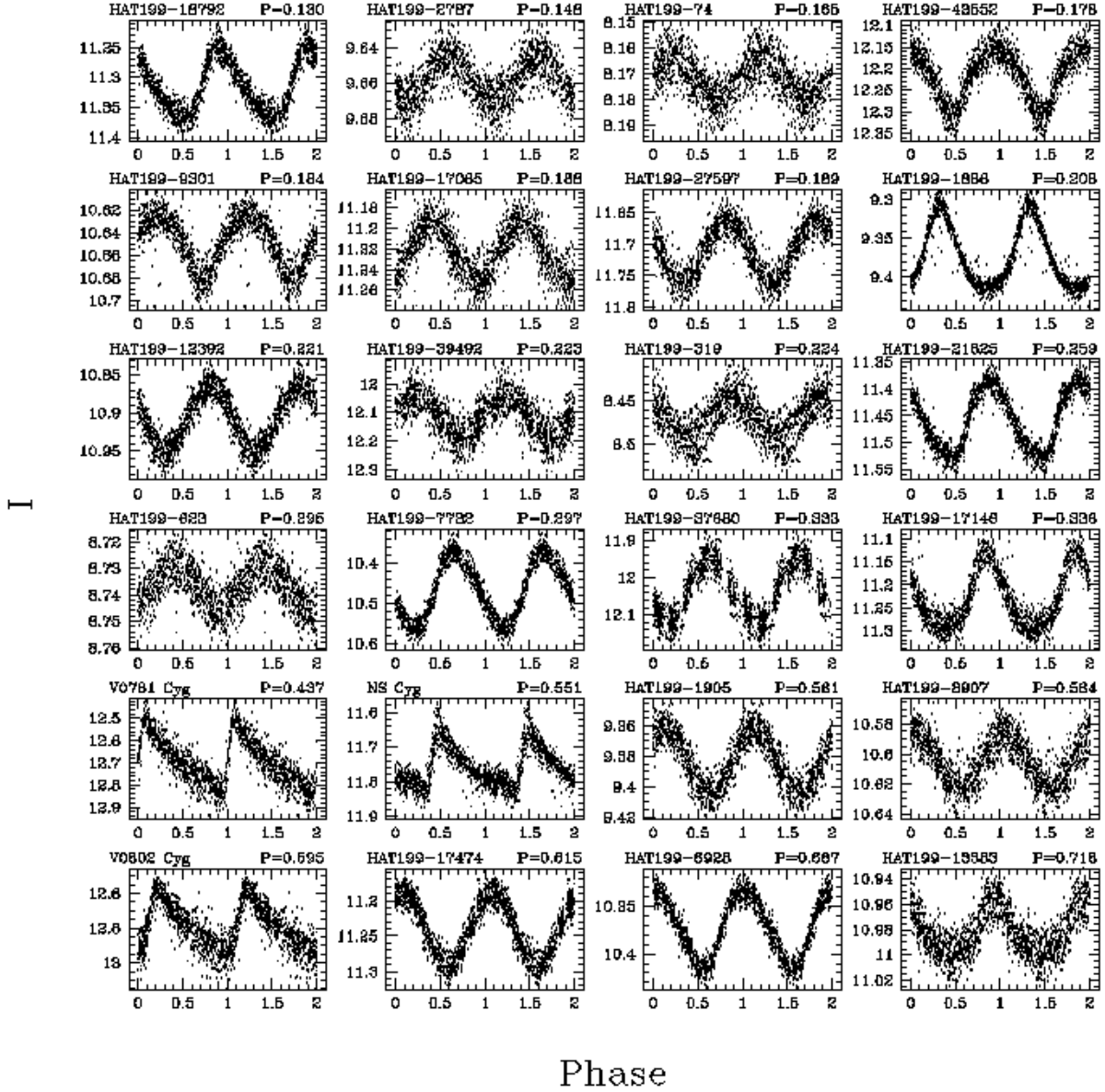


Fig. 14.— I-band light curves, sorted by period (given in days), for 48 of the 50 pulsating variables in our catalog. The other two are shown in Figure 17.

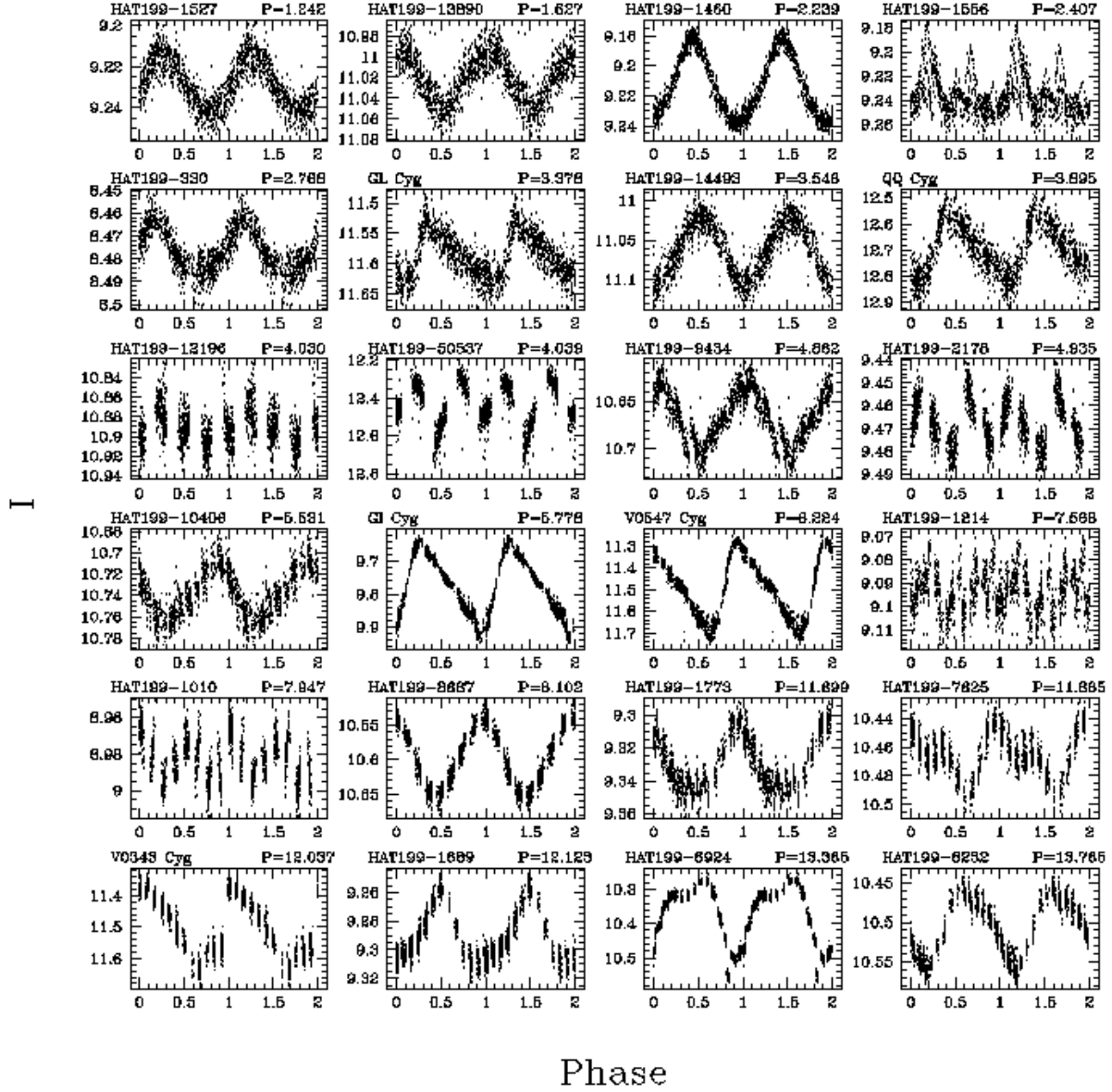


Fig. 14.— *Continued.*

Figure 15 shows the location of the periodic variables (separated into pulsating and eclipsing categories) on a J vs. J-K CMD. Compared to the LPVs and miscellaneous variables (Fig 12) these objects tend to be blue. For the pulsating stars this is expected as we are only classifying stars with periods less than 15 days as periodic, and the shorter period stars tend to be denser and hotter (e.g. δ Scuti).

The two most studied of the matched objects are WW Cyg, an EA/SD binary, and CV Cyg, a EW/DW binary. Because WW Cyg shows very deep primary eclipses (3.5 mag in V) it has been frequently observed over the last century. As a result this system has been particularly useful in probing the period changes in close binaries (Zavala et al. 2002). Our observations reveal much shallower eclipses in I (2.05 mag) and clearly reveal the secondary eclipses (0.15 mag in I) which have hitherto been undetected in V. Struve (1946) determined that the primary has spectral type B8, while Yoon et al. (1994) assigned a spectroscopic type G9 to the secondary. The difference of ~ 1.5 in the amplitude of the primary eclipse in V and I suggests that the secondary should have a later spectral type (later than K3). However Yoon et al. point out that the photometrically determined spectral types for Algol secondaries are typically later than the spectroscopically determined ones.

CV Cyg is a highly evolved eclipsing system that has been used primarily for the study of period and amplitude changes in close binaries (Demircan et al. 1995). Because the period is nearly 1 day (0.983 days) we do not observe both the primary and secondary eclipses, however we do obtain approximately 15 minima observations.

The light curve of one very interesting object that we observe is shown in Figure 16. This object matches the known EA/KE binary V1171 Cyg discovered by Wachmann (1966). It has also been detected as a visual double with $0''.34$ separation by Couteau (1981). The system has spectral type B9 as listed on SIMBAD. We obtain an orbital period for this system of $P=1.462$ d, and also observe an upper envelope modulation with period $P=4.857$ d and full-amplitude ~ 0.05 mag in I. To further analyze this system we obtained spectroscopy using the FLWO 1.5m telescope. The spectra show color changes, which indicate that this is not a random blend with another variable more than $1''$ away. The light curve appears to be very similar to HD227269 (§5.1 and Fig. 10), however in this case we have greater confidence that the pulsations and eclipses are occurring in the same system. We suspect that we are looking at a triple system with a Cepheid as one component. Evans et al. (2003) have found that a large fraction of Cepheids exist in triple systems, but have been unable to determine the masses of all 3 stars in a given system. If this system is indeed a triple, it may be possible to measure all three masses and thereby add to our picture of the distribution of masses among massive multiple systems (N. Evans, private communication).

We have also observed a number of objects which appear to be short period pulsating stars. These objects have periods between 0.1 and 0.3 days, and may well correspond to δ Scuti type variables. A number of these objects show multiple, non-harmonic periods. This includes HAT199-539 which appears to have at least two periods, one at 0.1069d and another at 0.1198d, and HAT199-5178 with periods at 0.1203d and 0.1367d (Fig. 17).

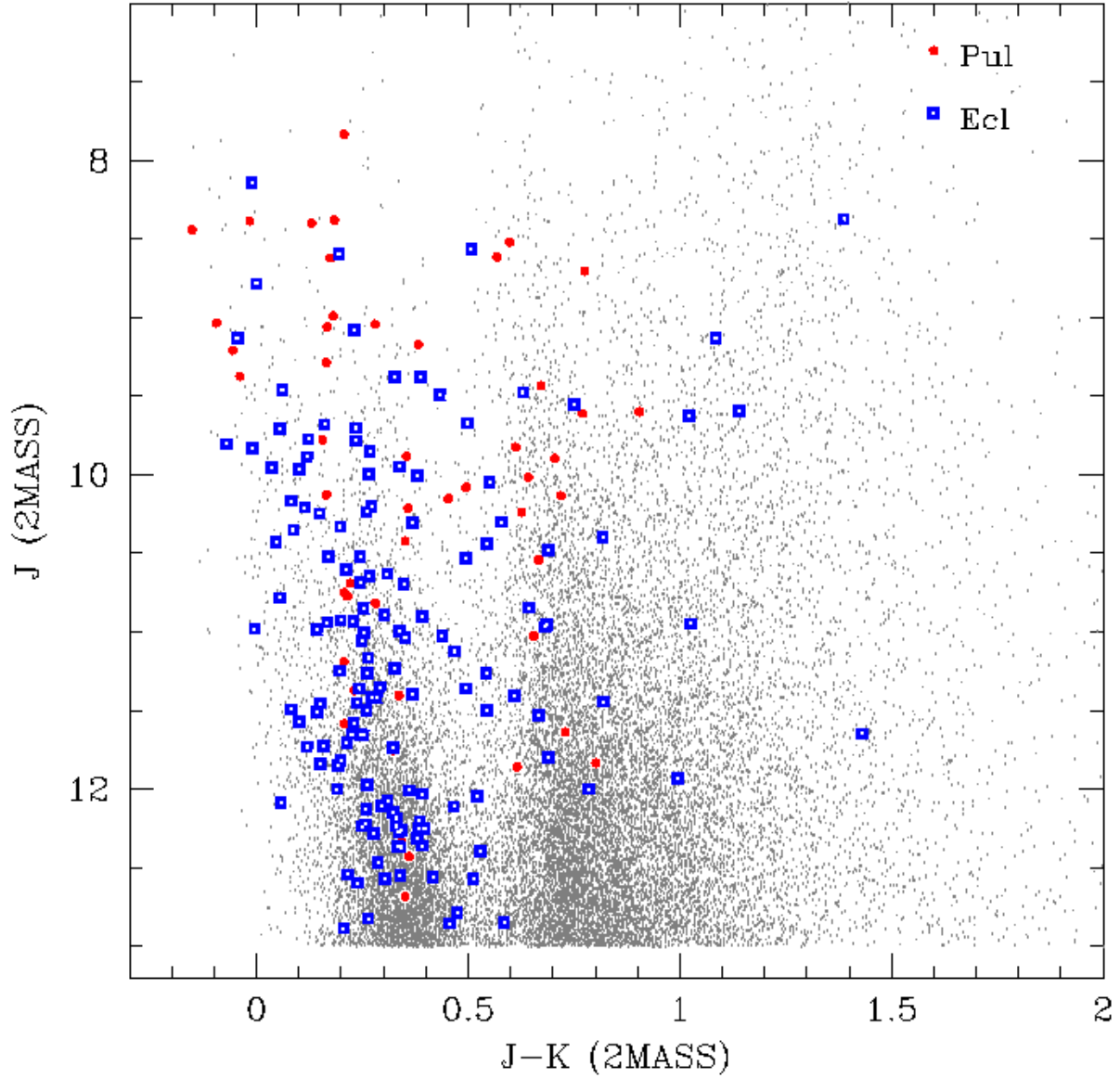


Fig. 15.— J vs. J-K CMD showing location of EB and pulsating variables relative to one tenth of the *2MASS* objects in our field with $J < 13$. Magnitudes are taken from *2MASS*. Note that the axis ranges are not the same as in Fig 12. Pulsating variables are shown as dots, EBs as squares, and the general population of objects is shown in grey. Note that both classes of periodic variables tend to lie toward the blue end (on the main sequence) relative to the LPVs and miscellaneous variables (Fig. 12).

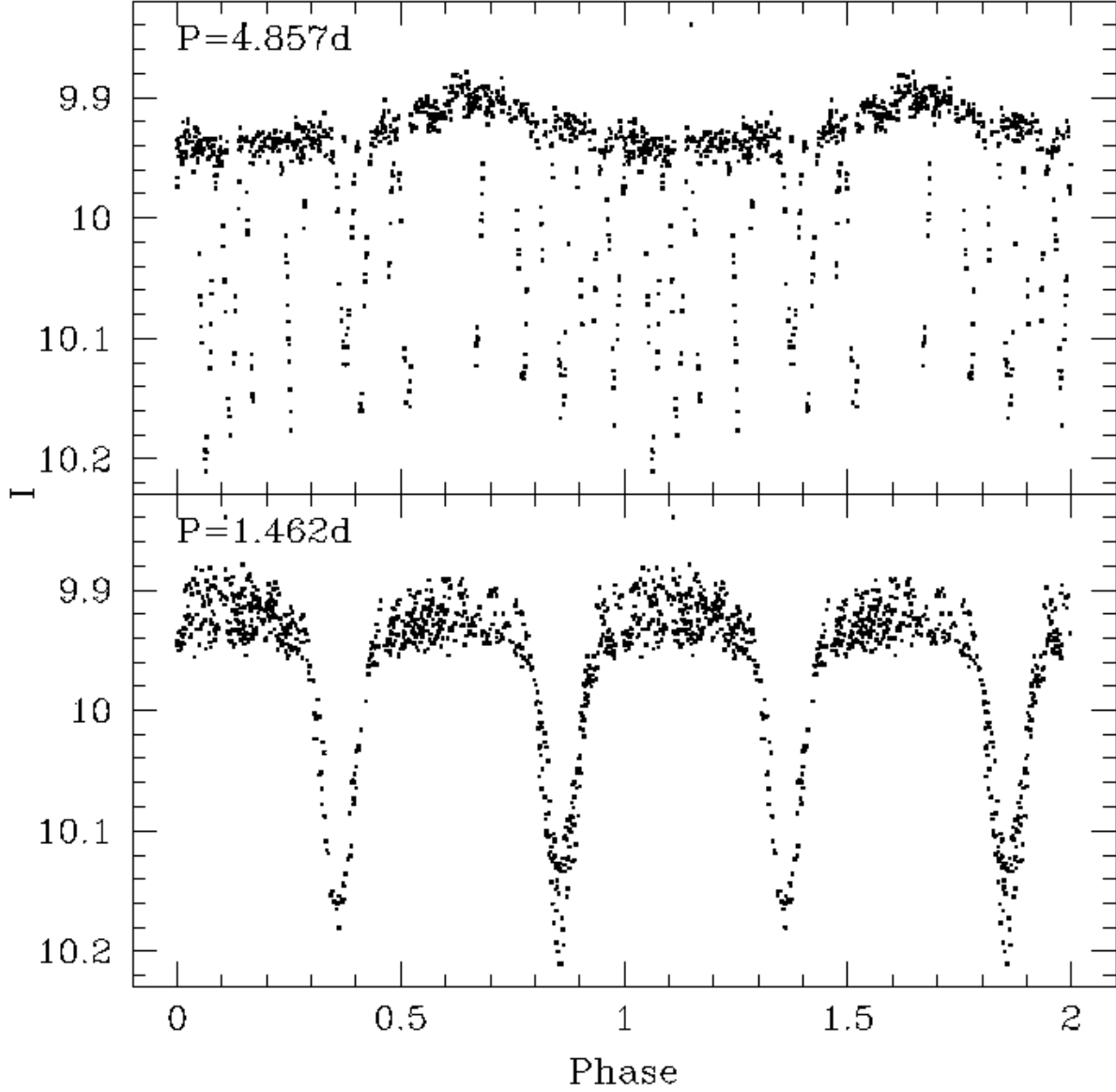


Fig. 16.— Light curve of V1171 Cyg shows eclipses with an orbital period of 1.462 days and a Cepheid-like upper envelope modulation with a period of 4.857 days (See discussion in §5.3).

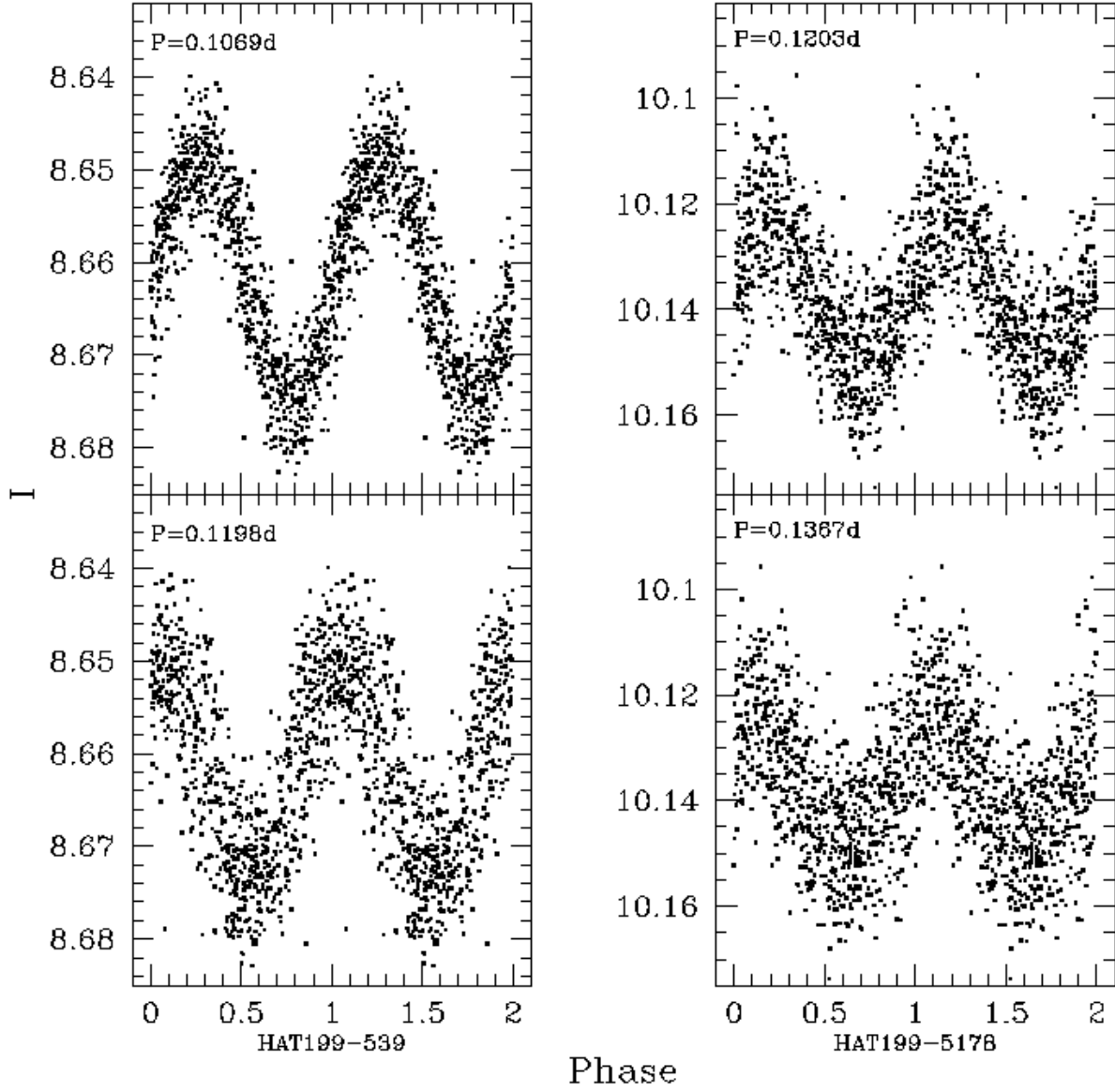


Fig. 17.— Light curves of HAT199-539 and HAT199-5178, two short period pulsating variables that show multiple, non-harmonic periods. (Left) HAT199-539 has periods of 0.1069d and 0.1198d. (Right) HAT199-5178 has periods of 0.1203d and 0.1367d.

5.4. Miscellaneous Variables

Variables which were not selected as LPVs and for which the best fit period was longer than 14 days were classified as miscellaneous. This classification may include a number of periodic variables with periods typically between 14-30 days, as well as a number of irregular variables that have timescales shorter than 30 days. We identified 241 such cases, of which all but 4 are newly discovered. The four matched cases include: V482 Cyg, an RCB star, V1920 Cyg, a PV Telescopii variable, V546 Cyg, an Algol-like eclipsing binary, and V811 Cyg, an SS Cyg type dwarf nova. Light curves of these, and other interesting miscellaneous variables are shown in Fig 18.

V482 Cyg is a well studied member of the rare class of stars known as R Coronae Borealis (RCB) variables. These carbon-rich variables are noted for their unpredictable and substantial drops in brightness that are attributed to the formation of soot clouds in the stellar atmosphere. V482 Cyg was in the quiescent state during the observations, however we do observe a pulsation-like light curve that suggests a period of around 30 days (Fig 18). This oscillation is very similar to the 39-day period, Cepheid-like pulsations observed in RY Sgr (see for example Lawson & Cottrell, 1990).

V1920 Cyg is an Extreme Helium Star which Morrison & Willingale (1987) observed to vary with an amplitude of 0.07 mag in V and a period of 3 to 4 days. Fadeyev (1990) interpreted these variations as pulsations in the second or higher overtone, and used them to constrain the absolute magnitude of the star. Our observations of V1920 Cyg over 30 days reveal irregular variations with no discernible period, but with a timescale of roughly 4 days. We observe a maximum full-amplitude of 0.2 mag in I (Fig 18). This variable is the bluest miscellaneous variable shown in Fig 12.

V811 Cyg is classified in the *GCVS* as a UGSS type variable. These stars are dwarf novae that show regular, symmetric outbursts typically lasting 3-10 days. We observe one such outburst for V811 Cyg with a time-span of roughly 10 days and amplitude of ~ 0.35 in I. It is interesting to note that our observations of V811 Cyg have a quiescent I of ~ 12.90 whereas Spogli et al. (2002) measured $I_c > 14.8$ in 1995. A likely interpretation is that we have observed a blend between V811 Cyg and another brighter source. Although the light curve we identify with V811 Cyg is one of the variables that does not have a match with *2MASS*, we do identify two sources in the full *2MASS* catalog that lie within $10''$ of our coordinates for the object. These sources have $J = 14.090$, $J = 15.397$, and $J - H > 0$. A blend of these two objects in DAOPHOT/ALLSTAR into a single object can account for the ~ 12.90 quiescent I. Note that the coordinates for V811 Cyg in the *GCVS* are more than $10''$ from our coordinates for the object.

One interesting miscellaneous variable that has not previously been detected as a variable is HAT199-1753 which shows a flare-like brightening by at least 0.08 mag over the course of 5 hours. Unfortunately the light curve is interrupted by several bad nights.

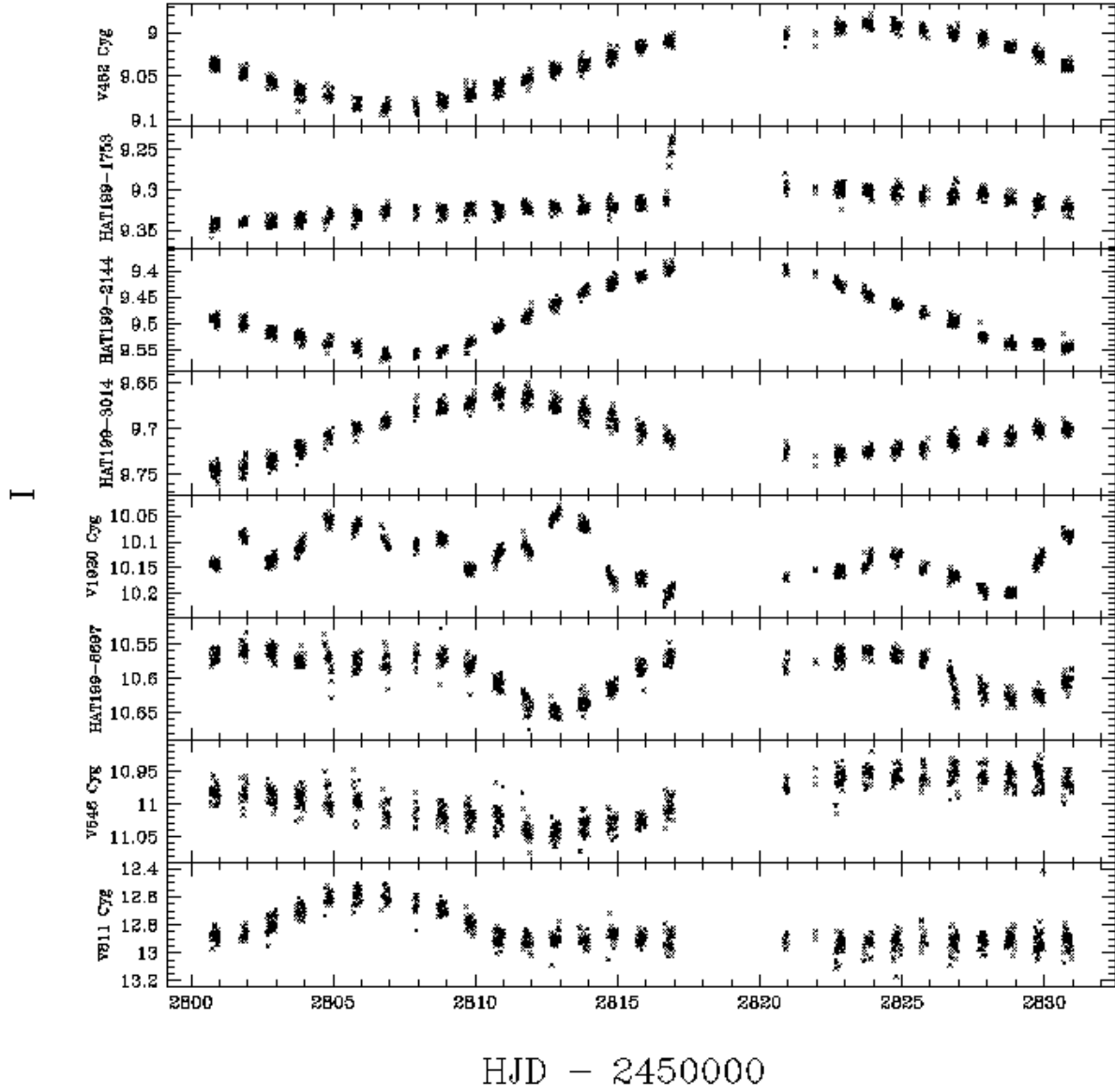


Fig. 18.— I-band light curves for 8 of the 240 miscellaneous variables in our catalog.

5.5. Low Amplitude Periodic Variables

As a test of our ability to detect very low amplitude periodic variables we performed the Schwarzenberg-Czerny period finding test (see §5.3) on the 8,949 light curves that had $RMS < 10$ mmag and $J_s < 1.0$. Using this scheme we selected an additional 71 light curves that had $P < 0.9$ days, and $\sigma_{AoV} > 3.5$ for the best period, and did not lie near the 1/2 or 1/3 harmonic of one day. We only selected objects that were more than 6 pixels from a variable in our catalog to avoid issues of variability blending. We then analyzed these light curves by eye and selected a list of 29 probable low-amplitude pulsating variables. We show light curves for a few of these in Figure 19, some of which have full-amplitudes approaching 10 mmag.

This is not a systematic search for these variables; we present the results simply to demonstrate our capability of finding very low amplitude variables in a high density field. We will continue observations of this field and present results from a systematic search for transits and other low amplitude variability in a future paper.

6. Conclusion

By using image subtraction photometry we have obtained light curves for over 98,000 objects in a single field near the galactic plane. From these light curves we have identified 1617 variable stars with amplitudes greater than ~ 0.032 mag, of which 1489 are new. These include 1072 new LPVs, 180 new periodic variables and 237 new miscellaneous variables. The fact that 92% of the variables were previously undetected further demonstrates the vast number of variables yet to be discovered even among fairly bright stars in our Galaxy.

We will continue our observations of this field in the hopes detecting planetary transits as well as other low amplitude variables by means of extending our baseline. Using rudimentary selection techniques we have already identified as many as 29 periodic variables with amplitudes less than 0.05 mag. Besides the detection of low-amplitude variables, future observations should also help in determining the nature of the variables we have already discovered.

We gratefully acknowledge G. Pojmanski for his excellent “lc” program, W. Pych for his “fwhm” program, J. Devor for his period-finding code, P. Berlind, M. Calkins, and T. Matheson for obtaining and analyzing spectra of V1171 Cyg, D. Latham and N. Evans for helpful discussion, and A. Bonanos and B. Mochejska for their help with the ISIS photometric package. We are grateful to C. Akerlof and the ROTSE project for the long-term loan of the lens used in the HAT-5 telescope. This research has made use of the SIMBAD database, operated at CDS, Strasbourg, France. JDH is funded by a National Science Foundation Graduate Student Research Fellowship. Partial support for the HAT project has been provided through NASA grant NAG 5-10854.

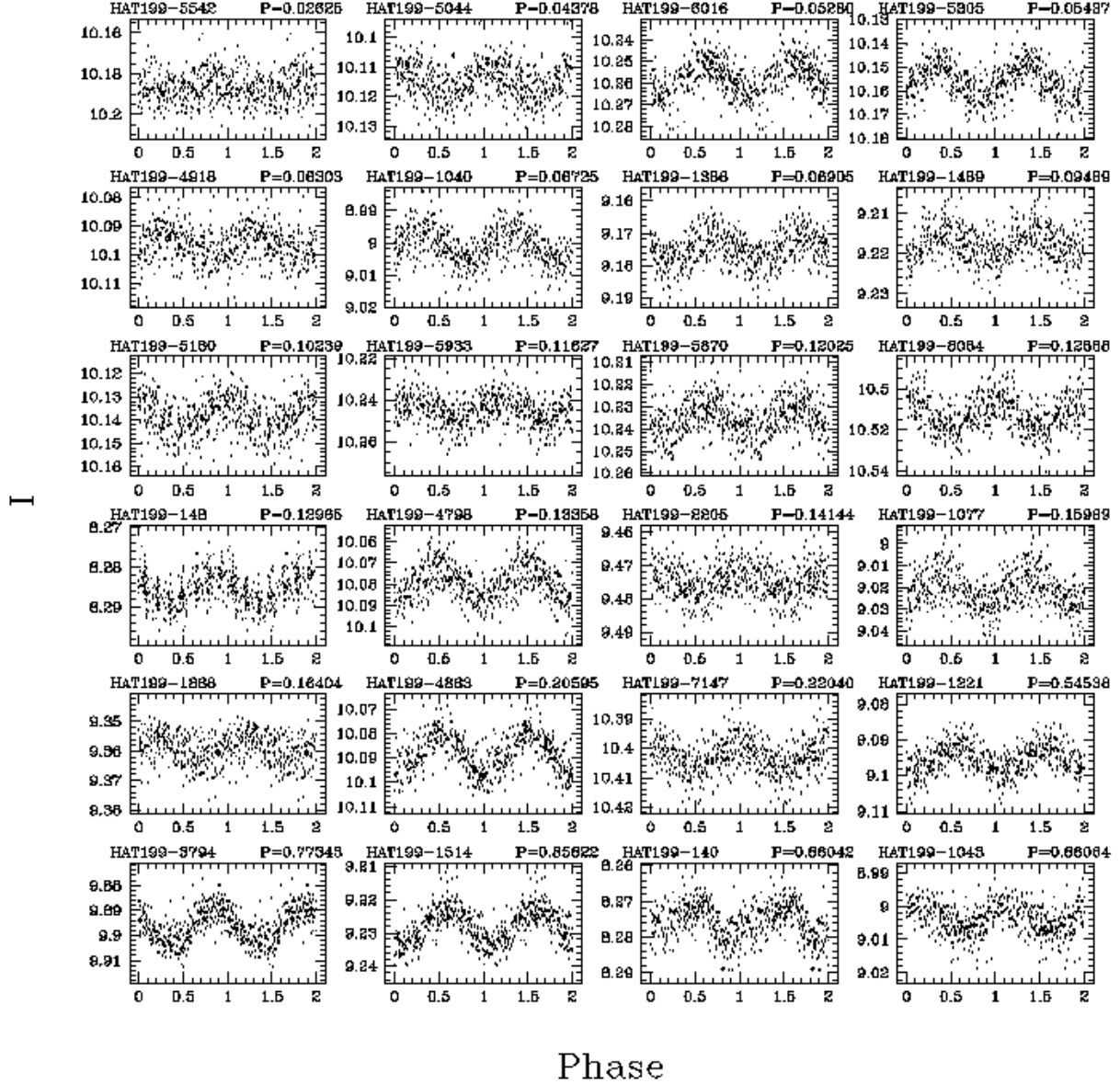


Fig. 19.— I-band light curves of 24 low-amplitude, periodic variables selected using the Schwarzenberg-Czerny algorithm. The light curves have been binned by 20 minutes to reduce the noise.

REFERENCES

- Alard, C., Lupton, R. 1998, *ApJ*, 503, 325
- Alard, C. 2000, *A&AS*, 144, 363
- Alonso, R., Belmonte, J. A., & Brown, T. 2003, *Ap&SS*, 284, 13
- Bakos, G., Noyes, R. W., Kovács, G., Stanek, K. Z., Sasselov, D. D., & Domsa, I. 2004, *PASP*, 116, 266
- Bessel, M. S. 1976, *PASP*, 88, 557
- Borucki, W. J., et al. 2001, *PASP*, 113, 439
- Borucki, W. J., et al. 2003, in *Proc. SPIE Vol. 4854, Future EUV/UV and Visible Space Astrophysics Missions and Instrumentation.*, eds, J. C. Blades, & O. H. W. Siegmund, SPIE, Bellingham
- Bouchy, F., Pont, F., Santos, N. C., Melo, C., Mayor, M., Queloz, D., & Udry, S. 2004, *A&A*, accepted (astro-ph/0404264)
- Couteau, P. 1981, *A&AS*, 43, 79
- Demircan, O., Mueyesseroglu, Z., Selam, S. O., Derman, E., & Akalin, A. 1995, *A&A*, 297, 364
- Evans, N. R., Carpenter, K. C., Robinson, R., Kienzle, F., & Dekas, A. 2003, *AAS*, 202, 3906
- Fadeyev, Y. A., 1990, *MNRAS*, 244, 225
- Friedemann, C., Guertler, J., & Loewe, M. 1996, *A&AS*, 117, 205
- Groenewegen, M. A. T., 2004, *A&A*, accepted (astro-ph/0404561)
- Horne, K. 2003, in *ASP Conf. Ser. 294, Scientific Frontiers in Research on Extrasolar Planets*, ed. D. Deming & S. Seager (San Francisco: ASP), 361
- Kaluzny, J., Stanek, K. Z., Krockenberger, M. & Sasselov, D. D. 1998, *AJ*, 115, 1016
- Konacki, M., Torres, G., Jha, S., & Sasselov, D. D. 2003, *Nature*, 421, 507
- Konacki, M., et al. 2004, *ApJL*, submitted (astro-ph/0404541)
- Lawson, W. A., & Cottrell, P. L. 1990, *MNRAS*, 242, 259
- Mochejska, B. J., Stanek, K. Z., Sasselov, D. D., Szentgyorgyi, A. H. 2002, *A&J*, 123, 3460
- Mochejska, B. J., Stanek, K. Z., Sasselov, D. D., Szentgyorgyi, A. H., Westover, M., Winn, J. N. 2004, *AJ*, submitted (astro-ph/0402306)
- Morrison, K., & Willingale, G. P. H., 1987, *MNRAS*, 228, 819
- Parimucha, S. 2003, *CoSka*, 33, 99
- Perryman, M. A. C., et al. 1997, *A&A*, 323, L49
- Safar, J., & Zejda, M. 2002, *IBVS*, 5263, 1S
- Schwarzenberg-Czerny, A. 1996, *ApJ*, 460, L107

- Skrutskie, M. F., et al. 1997, *The Impact of Large-Scale Near-IR Sky Surveys*, ed. F. Garzón, N. Epchtein, A. Omont, B. Burton, & P. Persei (Dordrecht: Kluwer), 25
- Spogli, C., et al. 2002, *IBVS*, 5240, 1S
- Stetson, P. B. 1987, *PASP*, 99, 191
- Stetson, P. B. 1992, *JRASC*, 86, 71
- Stetson, P. B. 1996, *PASP*, 108, 851
- Struve, O. 1946, *ApJ*, 104, 253
- Torres, G., Konacki, M., Sasselov, D. D., & Jha, S. 2004, *ApJ*, submitted (astro-ph/0310114)
- Udalski, A., Zebrun, K., Szymanski, M., Kubiak, M., Soszynski, I., Szewczyk, O., Wyrzykowski, L., & Pietrzynski, G. 2002, *Acta Astron*, 52, 115
- Udalski, A., Pietrzynski, G., et al. 2003, *Acta Astron.*, 53, 133
- Wachmann, A. A. 1966, *AAHam*, 6, 281
- Wood, P. R., Alcock C., Allsman R. A., et al. 1999, in: “IAU Symposium 191: AGB stars”, eds. T. Le Bertre, A. Lèbre & C. Waelkens, Kluwer Academic Publishers, ASP, p. 151
- Wood, P. R., 2000 *PASA*, 17, 18
- Wozniak, P. R., 2000 *AcA*, 50, 421
- Wozniak, P. R., et al. 2004, *AJ*, 127, 2436
- Yoon, T. S., Honeycutt, R. K., Kaitchuck, R. H., & Schlegel, E. M. 1994, *PASP*, 106, 239
- Zavala, R. T., et al. 2002, *AJ*, 123, 450

Table 1. HAT Catalog of “Kepler’s Field” Variables: first 8 columns.

ID [HAT199-]	α_{2000}	δ_{2000}	I	J	H	K	2MASS ID
00001	19 ^h 44 ^m 49 ^s .29	37°32′59″.6	07.787	05.601	04.760	04.251	1275.128417
00006	19 ^h 40 ^m 59 ^s .04	36°43′32″.8	07.959	04.039	02.999	02.461	1267.127829
00009	19 ^h 46 ^m 42 ^s .35	34°50′40″.6	07.989	05.097	04.212	03.875	1267.127829
00020	20 ^h 03 ^m 57 ^s .48	39°59′16″.7	08.063	05.494	04.491	04.093	1299.142572
00029	20 ^h 01 ^m 50 ^s .00	33°28′24″.0	08.090
00049	19 ^h 43 ^m 09 ^s .81	34°06′09″.6	08.137	06.050	05.146	04.785	1241.138907
00060	19 ^h 25 ^m 08 ^s .27	35°59′57″.9	08.151	08.142	08.171	08.154	1259.119674
00061	19 ^h 41 ^m 17 ^s .60	40°10′41″.9	08.154	06.758	05.819	05.538	1301.125923
00074	19 ^h 49 ^m 59 ^s .62	35°40′14″.5	08.173	07.833	07.700	07.627	1256.139193

Note. — Coordinates are from 2MASS where available, as are J, H, and K measurements. The first 9 entries in the catalog are presented here, the full catalog will be available with the electronic version of the refereed paper.

Table 2. HAT Catalog of “Kepler’s Field” Variables: first column and last 6 columns.

ID [HAT199-]	CLASS	I_{min}	I_{max}	P [days]	GCVS ID	GCVS CLASS
00001	LPV	07.987	07.642
00006	LPV	08.284	07.800	...	V942 Cyg	M
00009	LPV	08.024	07.917
00020	LPV	08.116	08.003	...	V423 Cyg	SRA
00029	LPV	08.172	08.052
00049	LPV	08.294	08.028
00060	ECL	08.275	08.044	01.4891
00061	MIS	08.179	08.124
00074	PUL	08.192	08.153	00.1650

Note. — Maximum and minimum I are the 6th from the brightest and dimmest measurements respectively. The first 9 entries in the catalog are presented here, the full catalog will be available with the electronic version of the refereed paper.